HAROLD WILLIAMS SERIES

The Timing of Strike-Slip Deformation Along the Storstrømmen Shear Zone, Greenland Caledonides: U–Pb Zircon and Titanite Geochronology

Benjamin W. Hallett[1], William C. McClelland[2], and Jane A. Gilotti[2]

[1]Department of Earth and Environmental Sciences
Rennselaer Polytechnic Institute
Troy, NY 12180, USA

[2]Department of Earth and Environmental Sciences
121 Trowbridge Hall, University of Iowa
Iowa City, IA 52242, USA
E-mail: jane-gilotti@uiowa.edu

SUMMARY
The Storstrømmen shear zone (SSZ) in the Greenland Caledonides is widely interpreted to have formed in a transpressional regime during sinistral, oblique collision between Baltica and Laurentia in the Silurian to Devonian. New mapping of the SSZ at Sanddal documents a 100 m thick, greenschist-facies mylonite zone cutting the eclogite to amphibolite-facies gneiss complex. We present U–Pb ion probe geochronology on zircon and titanite from a variety of lithologies that shows the SSZ was active from late Devonian to the Carboniferous (at least until 350 Ma). The age of thrusting in the foreland is not well known, but must be younger than the age of eclogite-facies metamorphism at ~400 Ma. It is, therefore, possible that contraction is the same age as strike-slip motion, and that transpression is a viable model. The timing of the SSZ is synchronous with dextral strike-slip displacement on the Germania Land deformation zone. Simultaneous displacement on sinistral and dextral, conjugate shear zones suggests that the SSZ is part of a strike-slip fault system that led to lateral escape of material northward (present day coordinates) during the waning stages of plate convergence between Laurentia and Baltica.

SOMMAIRE
La zone de cisaillement de Storstrømmen (SSZ) dans les Calédonides du Groenland est généralement comprise comme ayant été formée durant un régime de transpression sénestre lors de la collision oblique entre Baltica et Laurentie, du Silurien au Dévonien. Une nouvelle cartographie de la SSZ à Sanddal décrit une zone de 100 m d'épaisseur de mylonite au faciès des schistes verts qui recoupe un complexe de gneiss au faciès éclogite à amphibolite. Notre analyse géochronologique par sonde ionique U–Pb sur zircon et titanite sur diverses lithologies, montre que la SSZ a été active de la fin du Dévonien jusqu'au Carbonifère (au moins jusqu'à 350 Ma). L'âge du chevauchement dans l'avant-pays n'est pas bien connue, mais il doit être plus jeune que le métamorphisme au faciès d'éclogite à ~400 Ma. Il est donc possible que la contraction soit du même âge que le mouvement de coulissage, et que la transpression soit un modèle viable. La chronologie de la SSZ est synchrone au mouvement de coulissage dextre de la zone de déformation de Germania Land. Les déplacements simultanés, sénestre et dextre, sur des zones de cisaillement conjuguées permettent de penser que la SSZ fait partie d'un système de décrochement qui a engendré une éjection latérale de matériau vers le nord (selon les coordonnées actuelles) durant les stades de convergence des plaques Laurentie et Baltica.

INTRODUCTION
Transpression (Harland 1971) occurs in orogens that experience oblique convergence (e.g. Fitch 1972; DeMets et al. 1990) and generally results in partitioning of displacement into components of orogen-parallel strike-slip translation and orogen-normal shortening (e.g. Oldow et al. 1990; Molnar 1992; Tikoff and Teyssier 1994; Jones and Tanner 1995; Teyssier et al. 1995; Dewey et al. 1998; Lin et al. 1998). Many of the original field-based observations leading to transpressional models at the orogen scale were derived from the Caledonides (e.g. Harland 1971; Soper and Hutton 1984; Holdsworth and Strachan 1991; Soper et al. 1992). Interpretation of these studies in parallel with improved mathematical models (e.g. Sanderson and Marchini 1984; Fossen and Tikoff

Geoscience Canada, v. 41, http://dx.doi.org/10.12789/geocanj.2014.41.038

1993; Dutton 1997; Jones et al. 1997, 2004; Jiang and Williams 1998) in turn resulted in a series of tectonic models for development of the Caledonides that focus on the importance of transpression in a collisional orogen (Soper et al. 1992; Dewey and Strachan 2003). In constructing and evaluating these models, most of the discussion centres on the nature of the structural fabric, i.e. sinistral versus dextral transpression, and the general timing of fabric development (e.g. Soper et al. 1992). Rarely are the ages of specific elements in a partitioned system evaluated with respect to one another. This may be acceptable where observations of partitioning in transpressional shear zones are made at the scale of tens of metres (e.g. Tikoff and Greene 1997; Lin et al. 1998), but when discussing partitioning at the orogen scale, the coeval nature of the strike-slip and contractional components of the deformation should be demonstrated.

The Storstrømmen shear zone (SSZ) in the Greenland Caledonides has played a prominent role in developing models for sinistral transpression during the Paleozoic collision of Baltica and Laurentia (Holdsworth and Strachan 1991; Strachan et al. 1992, 1995; Dewey and Strachan 2003). Strike-slip displacement along the SSZ is inferred to have been coeval with thrust displacement in the foreland to the west (Fig. 1) on the basis of (1) the similar appearance and metamorphic grade of the mylonite zones of the SSZ and thrusts in the foreland, and (2) a gradational change in geometry between the folding in the hinterland and folding consistent with sinistral shear in the SSZ (Strachan et al. 1992; Smith et al. 2007). However, geochronologic evidence for the coeval development of thrusting and sinistral shearing is lacking. We present new structural data and U–Pb titanite geochronology that provide an estimate of the timing of deformation in the SSZ in the Sanddal area (78º05'N, 21º30'W). The results provide evidence that SSZ deformation was post-collisional, and did not play a significant role in the Scandian phase of the Caledonian collision (e.g. Dewey and Strachan 2003). In addition, this study advances models for exhumation of the high-pressure metamorphic rocks

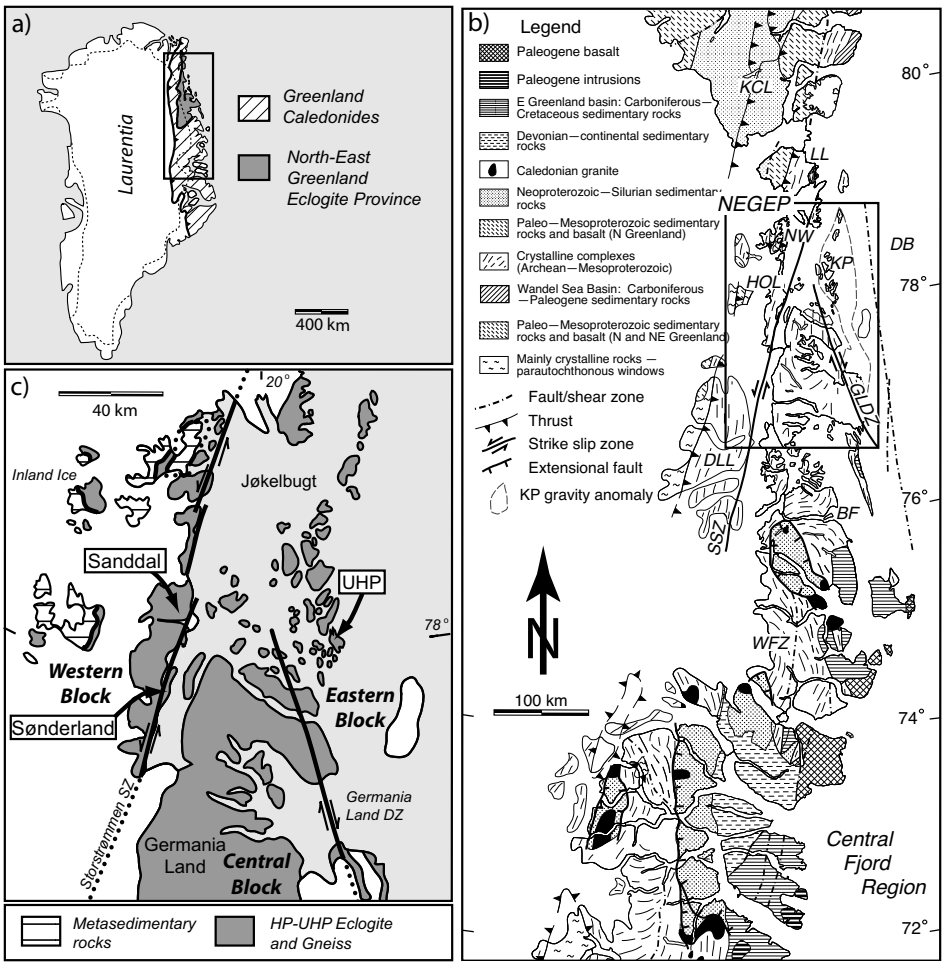

Figure 1. Geological map of the northern Greenland Caledonides showing the location of the North-East Greenland eclogite province (NEGEP), the sinistral Storstrømmen shear zone (SSZ) and the dextral Germania Land Deformation Zone (GLDZ) modified from Higgins and Leslie (2000). Additional abbreviations are: Bessel Fjord (BF), Dronning Louise Land (DLL), Kronprins Christian Land (KCL), Lambert Land (LL), Norreland window (NW), Hertugen af Orléans Land (HOL), Western fault zone (WFZ), Danmarkshavn Basin (DB), and Koldeway Platform (KP). Offshore features modified from Hamann et al. (2005).

of the North-East Greenland eclogite province by transpression in Devonian (Smith et al. 2007) to Carboniferous time.

GEOLOGIC SETTING

The East Greenland Caledonides form a 1300 km long, west-verging, fold-and-thrust belt that records the Paleozoic collision of Laurentia and Baltica (Fig. 1). The belt is characterized by thin-skinned, low-angle thrusts to the west and higher angle, thick-skinned deformation to the east (Higgins and Leslie 2008). There is also a fundamental difference in the orogenic architecture north and south of Bessel Fjord at 76°N (Gilotti et al. 2008). The metamorphic grade in the northern segment increases progressively in higher thrust sheets eastward toward the hinterland, where it reaches eclogite-facies conditions in the highest thrust sheet. South of 76°N, the sedimentary rocks of the foreland are structurally overlain by the deepest (highest pressure) level of the Laurentian crystalline basement, which in turn is overlain by a thrust sheet composed of mid-crustal level migmatitic gneiss, schist and peraluminous granite bodies. Neoproterozoic to Ordovician sedimentary rocks comprise the uppermost allochthon; Devonian and younger basins are developed on this substrate. The original thrust geometry is rearranged by syn- to post-orogenic extensional detachments south of Bessel Fjord

(Gilotti and McClelland 2008).

The thin-skinned thrust belt is discontinuously exposed in Dronning Louise Land, Lambert Land, and Kronprins Christian Land (Fig. 1b). Deformation in Kronprins Christian Land resulted in west-directed emplacement of Mesoproterozoic sedimentary rocks (Kalsbeek et al. 1999) over Neoproterozoic to Ordovician shelf strata and Silurian clastic rocks that are inferred to overlie Laurentian basement (Leslie and Higgins 2008). A foreland fold-and-thrust belt developed in the Paleozoic sequence marks the westernmost extent of Caledonian deformation. The influx of Silurian turbidites onto the Laurentian carbonate platform and their involvement in the thrust belt, with truncation of strata as young as Wenlock, are cited as evidence for the onset of the collision between Baltica and Laurentia (Hurst et al. 1983; Rasmussen and Smith 2001); however the timing of thrusting in the foreland is not well known.

The eastern hinterland north of 76°N is underlain by an orthogneiss complex, consisting of tonalitic to granodioritic gneiss, metagranitoid rocks and mafic plutonic rocks, which contain minor screens of metasedimentary rocks. The meta-igneous basement is largely Paleoproterozoic in age (Kalsbeek et al. 2008 and references therein), but rare Archean components are known (Nutman and Kalsbeek 1994). Mafic rocks, typically occurring as boudinaged layers and lenses, are widely distributed across the hinterland and record eclogite-facies metamorphism, defining the North-East Greenland eclogite province (NEGEP; Gilotti 1993). On the basis of data from the mafic pods, a large portion of the Paleoproterozoic gneiss units involved in the eastern thick-skinned belt experienced metamorphism at high pressure (HP) and locally ultrahigh-pressure (UHP) conditions (Gilotti et al. 2008). U–Pb SHRIMP zircon ages and Sm–Nd mineral isochron ages peg HP metamorphism between ~415–395 Ma (Gilotti et al. 2004), while the age of coesite-bearing zircon grains in the UHP belt ranges from 365–350 Ma (McClelland et al. 2006; Gilotti et al. 2014). The Norreland window exposes a thrust that places the eclogite-bearing orthogneiss complex over the Mesoproterozoic metasedimentary sequence. Thrusting must post-date the widespread eclogite-facies metamorphism in the uppermost thrust sheet that is as young as middle Devonian (Gilotti et al. 2004)—distinctly younger than the timing of deformation inferred from the Silurian turbidites in Kronprins Christian Land.

The hinterland is cut by two major shear zones that divide the NEGEP into western, central, and eastern blocks (Fig. 1c). The Storstrømmen shear zone (SSZ) records sinistral displacement and separates the western and central blocks (Strachan et al. 1992; Strachan and Tribe 1994). The timing of deformation along the SSZ is the subject of this contribution. The Germania Land deformation zone (GLDZ) records dextral displacement and separates the central and eastern blocks (Hull and Gilotti 1994). The GLDZ was active between 370 and 340 Ma, and responsible for partial exhumation of the eastern block (Sartini-Rideout et al. 2006). Timing of deformation within the SSZ and documentation of the continuity or disparity between both protolith ages and timing of metamorphism across it are required to evaluate the significance of the SSZ and its potential role in sinistral transpression models for the evolution of the Greenland Caledonides (e.g. Holdsworth and Strachan 1991; Strachan et al. 1995). We mapped a 12 km transect across the SSZ and surrounding gneiss at Sanddal, Hertugen af Orléans Land (~78°N; Fig. 2). Here we present the structural, petrologic and geochronologic results of our work. New U–Pb zircon and titanite dates clarify the protolith ages, timing of metamorphism, and age of deformation across and within the SSZ.

GEOLOGY OF THE SANDDAL REGION

The Gneiss Complex – Paleoproterozoic Protoliths and Caledonian Metamorphic History

The Sanddal region is composed of a heterogeneous suite of tonalitic to granodioritic orthogneiss, mafic rocks, leucocratic orthogneiss, garnet-bearing metagranite, granitic to tonalitic and trondhjemitic pegmatites, and minor garnet-rich paragneiss of the NEGEP (Fig. 2). The tonalitic to granodioritic orthogneiss is the prevalent lithology in the area and is derived from 2.0–1.8 Ga calc-alkaline intrusive complexes that represent a juvenile arc (Kalsbeek et al. 2008). The other units are either older screens of uncertain age or younger intrusions—mainly 1.75 Ga metagranitoid bodies—in the host orthogneiss. Deformation in the Sanddal area is characterized by a NNE-striking, subvertical regional composite gneissic foliation that records multiple periods of deformation and metamorphism. Mylonitic fabrics of the SSZ are superimposed on the regional gneissosity in the eastern portion of the field area (Fig. 2) and are discussed in the next section.

The polydeformed tonalitic to granodioritic orthogneiss is typically migmatitic and compositionally layered at the cm- to m-scale (Fig. 3a). The general assemblage is plagioclase + quartz ± alkali feldspar + biotite ± epidote ± zoisite ± clinozoisite ± hornblende ± white mica ± garnet with common accessory minerals of apatite, titanite, zircon, chlorite, and opaque minerals. Compositional banding is defined by alternating layers of quartzofeldspathic minerals and biotite ± hornblende ± epidote ± clinozoisite ± zoisite ± garnet and mm- to cm-thick leucosomes. The layering is cut by a large variety of m-scale trondhjemitic to granitic aplite and pegmatite veins, sills, and dikes. A ubiquitous gneissic foliation is defined by aligned biotite and rare white mica flakes, elongate feldspar, and quartz and feldspar aggregates and is sub-parallel to compositional layering. The foliation wraps around large (up to 1 cm) porphyroclasts of garnet, variably recrystallized feldspar augen, and centimetre- to metre-scale boudins of mafic and quartzofeldspathic protoliths. Isoclinal folds are defined by both the gneissic foliation and compositional layering.

Thin zones of paragneiss, generally less than 50 m thick, can be mapped along strike for a few kilometres at most (Fig. 2). Garnet–biotite schist and garnetiferous quartzite occur as discontinuous sheets. Small cm- to m-scale lenses of marble and calc-silicate rocks are locally preserved. The protolith ages are not known but these

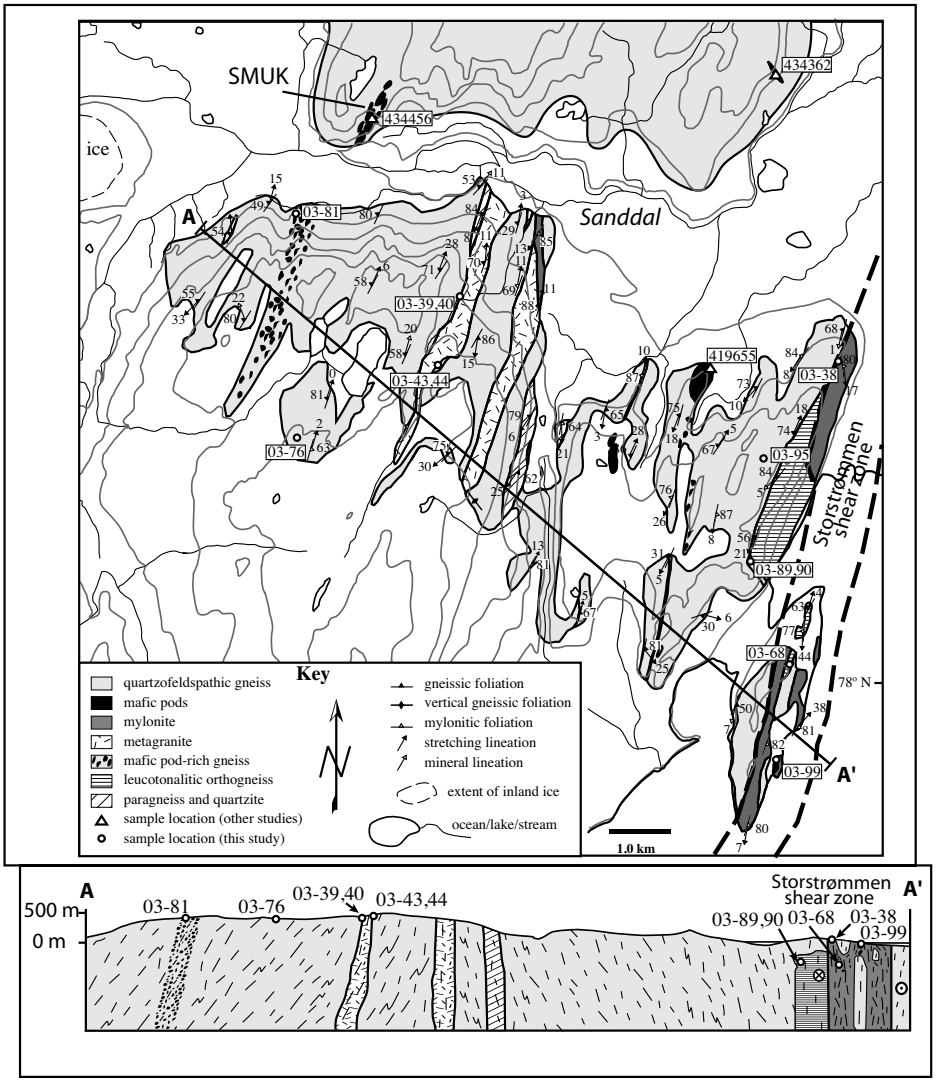

Figure 2. Geological map and schematic cross-section of the Sanddal area showing sample locations. SMUK is the Sanddal mafic–ultramafic complex.

units are interpreted as metasedimentary screens intruded by the calc-alkaline igneous complex. Paragneiss units with similar protoliths and contact relationships with the quartzofeldspathic host gneiss are present to the east in Germania Land (Hull et al. 1994).

Mafic HP rocks occur as lenses within quartzofeldspathic gneiss with individual pods typically 1–20 m in their long dimension (Fig. 3b); several larger eclogitic bodies are up to 500 m long (Fig. 2). The largest eclogitic bodies in the area are the Sanddal mafic–ultramafic complex (Lang and Gilotti 2001) and a leucogabbro with well-developed partial melt textures (Gilotti et al. 2004) in the western and eastern portions of the map area, respectively. In addition, pods often occur in trains extending several km along strike, suggesting they represent boudinaged dikes or screens within the quartzofeldspathic gneisses. The mafic lenses comprise bimineralic eclogite, rutile eclogite, quartz–rutile eclogite, and zoisite–kyanite–quartz–rutile eclogite. The large zoisite eclogite body (at sample 419655, Fig. 2) yielded a $^{207}Pb/^{206}Pb$ zircon age of 1962 ± 27 Ma for the leucogabbro protolith (Gilotti et al. 2004). Most mafic pods are variably amphibolitized; no *P-T* estimates are yet available for the western block. Estimates from the HP portion of the NEGEP in the central block indicate metamorphism at peak conditions of ca. 750°C and 1.5–2.2 GPa (Brueckner et al. 1998; Elvevold and Gilotti 2000). The mafic rocks typically have an internal foliation defined by the preferred orientation of omphacite, biotite ± zoisite that is commonly discordant to the regional fabric.

The host gneiss is intruded by several mappable metagranitoid sheets up to 500 m thick, as well as many smaller scale pegmatites (Fig. 2). Two bodies of the 1.75 Ga garnet-bearing metagranite were mapped in the centre of the area (Fig. 3c). A leucotonalitic orthogneiss is present as kilometre-scale discontinuous lenses west of and within the SSZ (Fig. 2). The leucotonalite bodies are correlative with the 'mylonitic leucogranite' unit mapped within the SSZ south of Sanddal in Sønderland (Strachan and Tribe 1994). Contacts of the intrusive bodies are generally parallel to the gneissic layering in the adjacent rocks, but cross-cutting relationships are locally preserved. Both the leucotonalitic orthogneiss and garnet-bearing metagranite lack significant migmatitic and gneissic compositional layering, but do have a penetrative foliation defined by alignment of biotite, elongate feldspar, and quartz–feldspar aggregates, also preserving a strong quartz or feldspar stretching lineation. Dikes of leucotonalitic orthogneiss cut isoclinal folds in the host gneiss and are themselves isoclinally folded. This type of folding is absent from the garnet-bearing metagranite bodies. Smaller granitic to tonalitic and trondhjemitic pegmatites occur 1) in the boudin necks of mafic pods, 2) as dikes several metre-thick that crosscut gneissic banding and foliation in the adjacent units but are foliated as well, and 3) centimetre- to metre-thick granitic dikes emplaced within shear zones or across foliation at high angles. The variety of cross-cutting relationships suggests that multiple intrusive and deformational events affected the tonalitic to granodioritic host gneiss. Similar relationships have been described regionally and were interpreted to represent both a composite Paleoproterozoic and Caledonian fabric in the tonalitic gneiss units, and a single Caledonian fabric in the garnet metagranite bodies (Hull et al. 1994). For this and geochemical reasons, the 1.75 Ga garnet granitoid rocks are commonly considered to be anorogenic (Kalsbeek et al. 2008).

Gneissic foliation and schistosity in the Sanddal area generally strike to the NNE with steep dips to

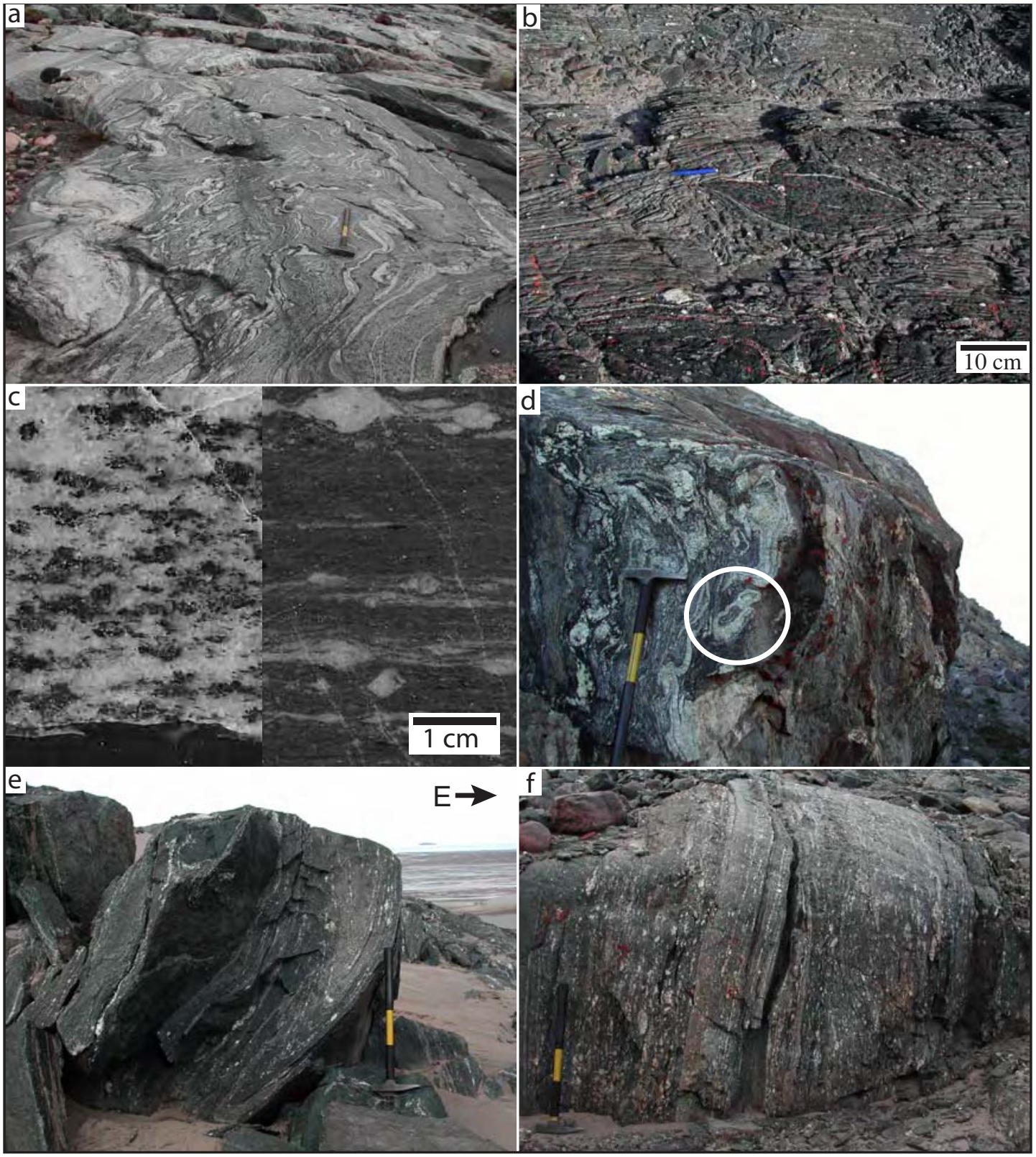

Figure 3. Photographs illustrating lithologies and structures in the gneiss complex and Storstrømmen shear zone (SSZ) at Sanddal; 0.5 m long rock hammer for scale in a, d–f. (a) Ptygmatic folding of leucocratic melt layers in orthogneiss. (b) Small-scale, σ-shaped eclogite lens wrapped by flaggy mylonitic foliation gives a sinistral sense of shear. (c) Rock slab images of garnet metagranite with simple, gneissic foliation (left) and mylonitic fabric (right). (d) Intensely folded gneiss within SSZ. Circled area shows concentric fold closure suggesting sheath folding. (e) Isoclinally folded, mylonitized gneiss within the SSZ; note bend in axial plane. (f) Quartzofeldspathic protomylonite and augen mylonite in the SSZ derived from the tonalitic to granodioritic gneissic protoliths.

the NW and SE (Fig. 4) and, with the exception of the mafic lenses, is defined by amphibolite-facies or lower grade assemblages. The compound planar fabrics are likely both Proterozoic and Paleozoic in age, but a distinction is difficult on the basis of outcrop-scale observation alone. The foliations contain shallowly plunging stretching and mineral lineations (Fig. 4). Stretching lineations defined by quartz ± feldspar aggregates and feldspar grains are collinear with amphibole, epidote, and clinozoisite mineral lineations that plunge shallowly to the NNE or SSW (Fig. 4). Zoisite and kyanite mineral lineations in mafic pods characteristically have a steep plunge indicating that the shallow plunging amphibolite-facies lineations post-date HP metamorphism. Folding in the gneiss is characterized by isoclinal folds of the gneissic foliation and compositional layering. Hinge lines of these folds are variable in orientation, but most commonly plunge shallowly to the NNE or SSW and are generally collinear with the regional stretching and mineral lineations (Fig. 4). Rare sheath folds observed as fully closed geometries in gneissic banding are observed at Sanddal in proximity to the SSZ (Fig. 3d; Strachan and Tribe 1994; Strachan et al. 1995). It is not demonstrable to what extent this geometry records superposition. Complex fold geometry is observed in proximity to mafic pods as well. The amphibolite-facies foliation, together with the mafic pods and associated Caledonian pegmatites, are folded into NE-trending upright folds that are also observed at the regional scale (Hull et al. 1994). These younger folds formed after the development of the older compound deformational fabrics and prior to or synchronous with the SSZ.

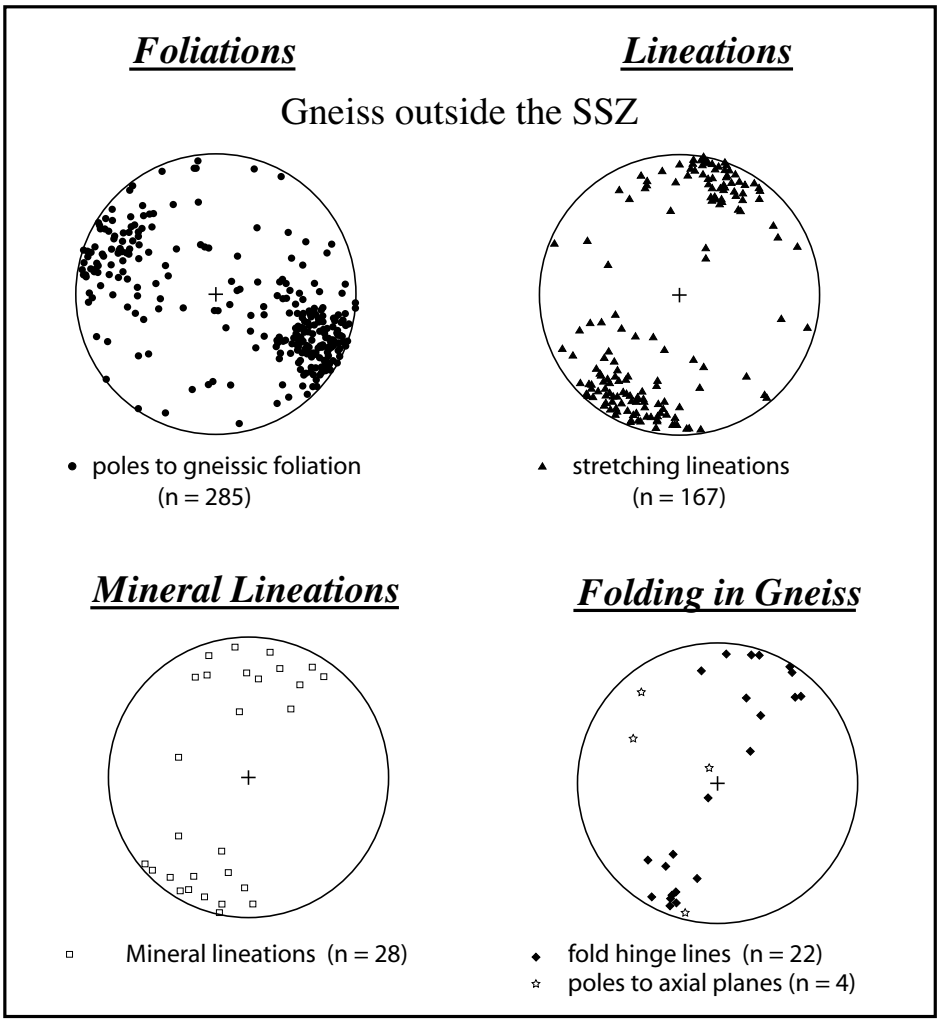

Figure 4. Lower hemisphere, equal area stereonets of structural data from the gneiss complex surrounding the Storstrømmen shear zone at Sanddal.

The Storstrømmen Shear Zone and Related Mylonite Zones

The SSZ at Sanddal consists of anastomosing mylonite zones up to 100 m thick that run along the easternmost shore exposures of the field area (Fig. 2). The shear zone in Hertugen af Orléans Land has been variably described as a zone with an exposed thickness of > 5 km (Strachan and Tribe 1994; Smith et al. 2007) to 1.8 km (Hull and Gilotti 1994). We mapped the western margin of the SSZ where zones of protomylonite to ultramylonite constitute > 50% of the outcrop. Widely spaced mylonitic shear zones, ranging from several centimetres to several metres thick, occur west of the SSZ and are interpreted to have formed during the same deformation event. The eastern SSZ boundary is concealed beneath Jøkelbugt.

Using the classification scheme of Sibson (1977), rocks of the SSZ and related shear zones range from protomylonitic gneiss to ultramylonite (Fig. 3e, f). Mylonitic foliations strike to the NNE and generally have a steeper dip than the regional gneissic fabric (Fig. 5). Within the SSZ, screens of gneiss and amphibolite are surrounded by anastomosing mylonite zones. These low strain volumes exhibit a gneissic fabric that is commonly rotated into concordance with the surrounding mylonitic foliation. Most of the mylonite zones are characterized by a quartz + feldspar + mica matrix with porphyroclasts of epidote, zoisite, clinozoisite, feldspar, titanite, and garnet. Mylonitization involved growth and recrystallization of biotite, white mica, chlorite, quartz, epidote, clinozoisite, and feldspars. Some zoisite or clinozoisite cores have epidote rims that are interpreted to have formed during mylonitization. Amphibole is retrogressed and only occurs in mylonite zones outside of the main SSZ, and very rarely as a trace mineral in the SSZ ultramylonite. Where present, amphibole is partially replaced by biotite + epidote + clinozoisite + titanite, all of which occur as porphyroclasts in the mylonitic fabric. The scarcity of stable amphibole suggests that in most rocks it was completely replaced by subsequently deformed

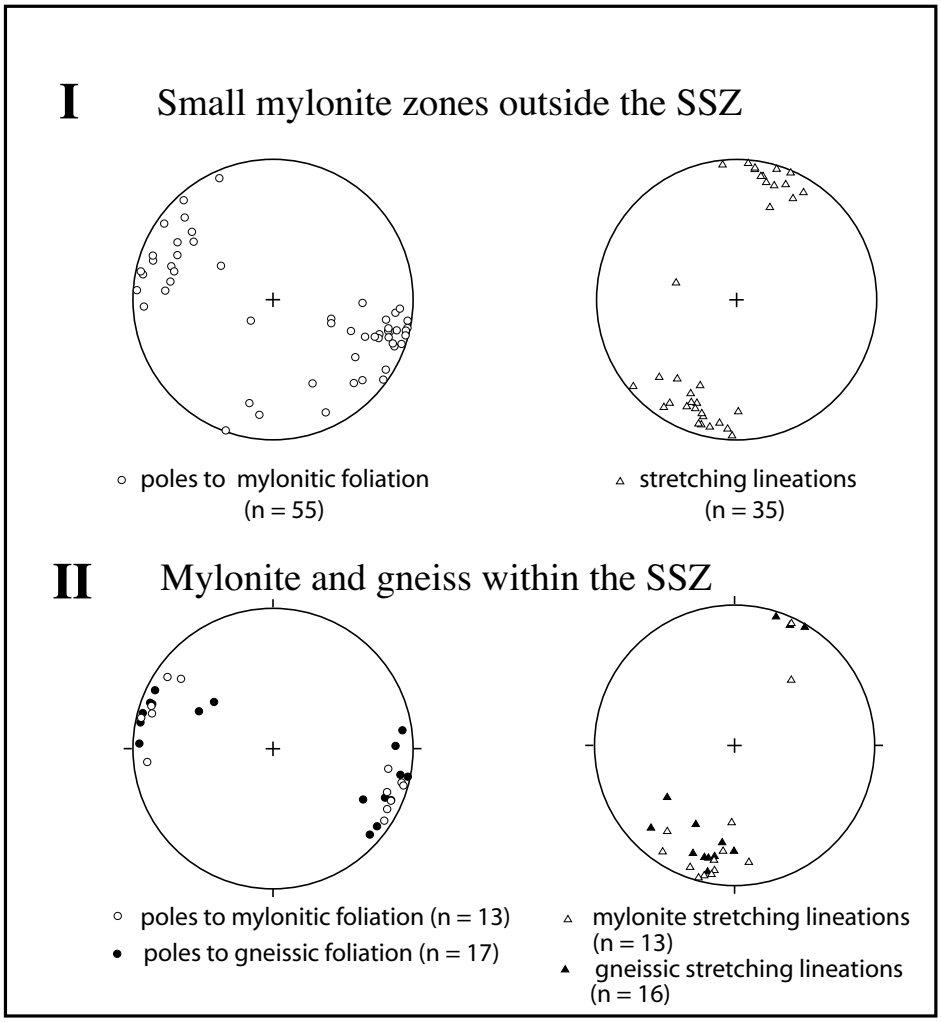

Figure 5. Lower hemisphere, equal area stereonets of structural data from mylonitic gneisses within and outside of the main Storstrømmen shear zone at Sanddal.

lower grade minerals, and hence mylonitization occurred at greenschist-facies conditions. This is consistent with growth of epidote rims and chlorite adjacent to pristine biotite in the mylonitic fabric and shear bands.

The mylonitic foliation within the SSZ, as well as in gneiss outside the SSZ, is partly defined by polycrystalline quartz and feldspar ribbons. The long axes of feldspar augen, garnet, and epidote grains generally lie within the mylonitic fabric (Fig. 6a). Biotite-rich, spaced shear bands obliquely cut the mylonitic fabric (Fig. 6b). Spacing of mylonitic foliations is on the scale of 100–500 μm. In quartz-rich mylonite, quartz subgrains form an oblique fabric between spaced bands of the main, mica-defined mylonitic fabric. Isoclinal folding of the mylonitic fabric is also observed within the SSZ. Similar relationships are described in Dronning Louise Land (Holdsworth and Strachan 1991; Strachan et al. 1992). These structures are interpreted as oblique folds related to shearing on the SSZ.

Lineations formed by stretching and constriction of quartz and feldspar grains occur in the gneissic and mylonitized rocks (Fig. 5). Mineral (shape-preferred) lineations, defined by amphibole, epidote, zoisite, clinozoisite, and elongate garnet, are also found in the gneiss. Outside of the SSZ, stretching and mineral lineations plunge shallowly to the SSW and, in some places, to the NNE. This SSW preference in stretching lineation plunge is more pronounced in mylonite, ultramylonite, and gneissic screens within the SSZ. As stretching and mineral lineations in mylonite and in the host gneiss are subparallel, it is unclear whether any linear fabric is preserved from previous regional deformation or formed during shearing related to the SSZ.

Polycrystalline quartz ribbons show an orthorhombic symmetry and are flattened with aspect ratios of 1:5 viewed in lineation-normal cross sections. In sections cut parallel to the lineation and perpendicular to the foliation, quartz ribbons have aspect ratios of 1:4 up to 1:10. Because pre-deformational quartz grain geometry is not known, estimates of finite strain are speculative at best. Nevertheless, the 3-dimensional polycrystalline quartz ribbon geometry is estimated to reflect non-plane strain within a non-coaxial flow regime. Augen show a fairly regular geometry in thin section. Elongate feldspars commonly develop recrystallized mantles and tails that define σ-type sinistral shear sense indicators in lineation-parallel, foliation-normal cuts. In lineation-normal cuts, these feldspar augen show orthorhombic shape symmetry, and often show oblate cross sections with aspect ratios of 1:2. Elongate epidote, zoisite, clinozoisite, amphibole, and titanite porphyroclasts show orthorhombic symmetries in lineation-parallel cuts. However, biotite and white mica in external tails on these porphyroclasts exhibit stair-stepping with a sinistral asymmetry. Lineation-normal cross sections of these porphyroclasts show the same geometry as feldspar.

Macro- to micro-scale shear sense indicators are observed in most mylonitic rocks, as well as in sheared host gneiss. These include σ- and δ-type porphyroclasts, shear bands, oblique quartz subgrain fabric, and mica fish (Fig. 6c). Field observations revealed dominantly sinistral shear sense indicators, in agreement with previous studies (Holdsworth and Strachan 1991; Strachan et al. 1991; Hull and Gilotti 1994; Strachan and Tribe 1994). Eight mylonite and ultramylonite examples from within the SSZ show sinistral microscopic shear sense indicators, while 11 of 12 mylonite and protomylonite examples from outside the SSZ show sinistral shear sense. Microscopic shear bands and augen asymmetry in 3 of 3 sheared gneiss examples also show sinistral shear

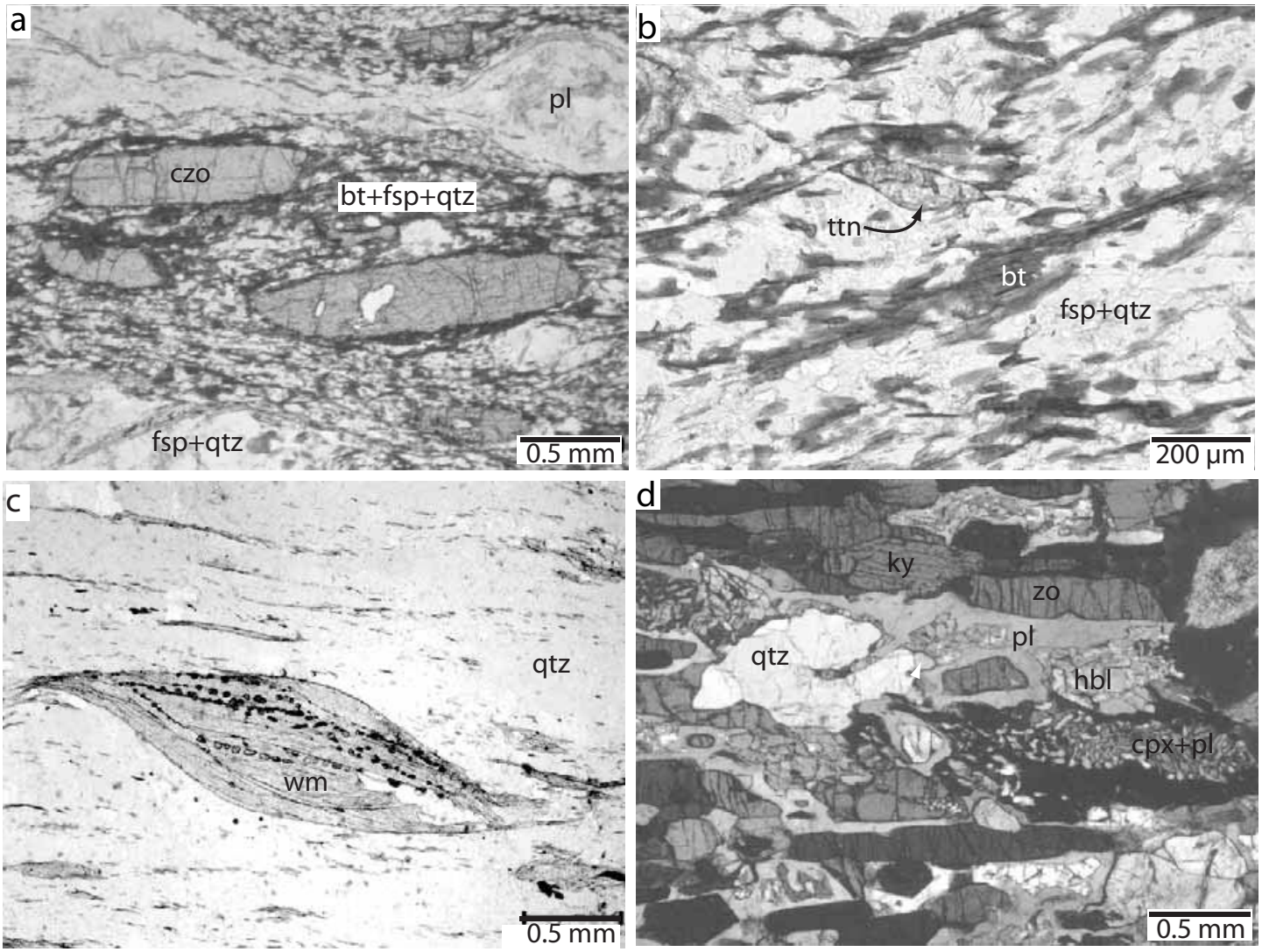

Figure 6. Plane-polarized (PPL) and crossed polars (XP) photomicrographs of selected metamorphic tectonites. (a) Clinozoisite grains with long axes parallel to mylonitic foliation defined by grain-shape-preferred orientation of biotite, feldspar, and quartz in the matrix, 03-29 (PPL). (b) Fish-shaped titanite grain deformed by biotite-rich shear bands showing the sinistral shear sense in a SSZ mylonite, 03-38 (PPL). (c) White mica fish indicating sinistral shear within a mylonitized paragneiss, 03-33 (PPL). (d) Zoisite + kyanite eclogite showing clinopyroxene + plagioclase symplectite replacing omphacite, parallel to a zoisite-defined fabric, 03-99 (XP). Abbreviations are after Whitney and Evans (2010), in addition wm = white mica and qtz = quartz.

sense.

Significant hydrothermal alteration has affected some of the mylonite areas within the SSZ. Chloritization of biotite, sericite growth within and adjacent to feldspar, and a cloudy appearance of some feldspar grains, interpreted to represent breakdown to clay minerals, are common. Hydrothermal alteration features have developed preferentially along layers in the finest grained ultramylonite from the core of the SSZ. Other evidence of hydrothermal alteration includes growth of secondary calcite in fractures in some SSZ mylonite.

U–Pb GEOCHRONOLOGY

Zircon and titanite separates were analyzed from representative samples of eclogite, gneiss, leucocratic intrusions and mylonite in order to establish the timing of Caledonian metamorphism and deformation within and outside the SSZ.

Methods

Zircon and titanite grains were extracted from 0.5–3.0 kg samples and analyzed for U–Pb on the SHRIMP–RG (sensitive high resolution ion microprobe–reverse geometry) instrument at the United States Geological Survey–Stanford University Microanalytical Center, Stanford, CA. Grains were separated using standard magnetic and gravimetric techniques and then hand-picked under alcohol. Whole zircon grains were selected on the basis of clarity and lack of fractures. Titanite was selected on the basis of magnetic susceptibility, colour, and lack of inclusions. All grains were mounted in epoxy and polished to expose grain interiors. Cathodoluminesence (CL) images of zircon and backscattered electron (BSE) images of titanite were used to characterize grains prior to analysis. Concentrations of U were based on analyses of standard CZ3 (550 ppm) for zircon and BLR1 (250

ppm) for titanite. Isotopic compositions were calibrated by replicate analyses of zircon standard R33 (421 Ma; Black et al. 2004; Mattinson 2010) and titanite standard BLR1 (1047 Ma; Aleinikoff et al. 2007). Calibration errors for the $^{206}Pb/^{238}U$ ratios of R33 for the three different analytical sessions were 0.45%, 0.47% and 0.51% (2σ). Calibration error for the $^{206}Pb/^{238}U$ ratios of BLR1 was 0.65% (2σ). The analytical routine followed procedures outlined in Barth and Wooden (2006), while data reduction and plotting was done using programs of Ludwig (2001, 2003).

The samples record a complex Proterozoic and Paleozoic igneous and metamorphic history. The interpretation of the zircon and titanite U–Pb data varies as a function of age, observed systematics, and removal of the common Pb component prior to age calculation. Most of the Proterozoic zircon analyses are discordant due to Caledonian disturbance; therefore, Proterozoic ages are calculated from a two-dimensional regression of ratios corrected by the ^{204}Pb method using common Pb compositions estimated from Stacey and Kramers (1975) and an observed or assumed lower intercept age of ca. 395 Ma. Paleozoic zircon domains yielded concordant to discordant analyses with discordance due to common Pb, inherited components, or both. Ages for Caledonian zircon are based on weighted mean ages of analyses inferred to represent a single age component and corrected by the ^{207}Pb method (Williams 1998). Titanite analyses have highly variable common Pb abundances, ranging from 4 to 85% of the total Pb and reflected by $^{206}Pb/^{204}Pb$ ratios between 1,410 and 18.6. The common Pb correction was made using the measured $^{206}Pb/^{204}Pb$ ratios and the 3-dimensional total Pb method of Ludwig (1998). Interpretation of analyses inferred to contain two components of radiogenic Pb in addition to common Pb used the planar solution in Isoplot (Ludwig 2003). The linear solution (Ludwig 2003) was used for samples interpreted to represent a simple mixture of common and radiogenic Pb in Paleozoic titanite.

U–Pb Zircon Geochronology for the Sanddal Area

Samples were collected from zoisite–kyanite eclogite, garnet metagranitoid rock, and several pegmatites (Fig. 7). Sample locations are shown in Figure 2 and the mineralogy of the samples is given in Table 1. Cathodoluminescence (CL) images of selected zircon grains from dated samples are presented in Figure 8, Tera–Wasserburg plots of the U/Pb ages are given in Figure 9, and U–Pb geochronologic data and calculated ages for zircon are presented in Table 2.

Sample Descriptions and Results

Retrogressed zoisite–kyanite eclogite, 03-99, is a lens within mylonitic gneiss of the SSZ (Fig. 7a). The sample consists of approximately 35% zoisite, 25% omphacitic pyroxene, 10% amphibole, 5% kyanite, 5% garnet and 10% retrograde plagioclase. Rutile and zircon are important accessory phases. A well-developed foliation is defined by parallel alignment of zoisite needles (up to 4 mm long), kyanite, omphacite and compositional layering defined by felsic layers composed mainly of deformed plagioclase. Zircon from this eclogite has very low U (1–16 ppm) and Th/U (0.002–0.07) metamorphic overgrowths on oscillatory zoned, higher U (71–2960 ppm) and Th/U (0.09–0.36) cores (Fig. 8a). The rim $^{206}Pb/^{238}U$ ages range from 545 to 269 Ma. Inferring that the oldest rim analysis reflects a mixture of rim and core material and the 4 younger analyses reflect continued growth and/or Pb loss, the remaining 12 analyses give a weighted mean $^{206}Pb/^{238}U$ age of 394 ± 12 Ma (MSWD = 0.7; Fig. 9a). The large uncertainty induced by low U and Pb concentrations precludes a finer resolution. It is possible that zircon growth in this sample may have spanned HP metamorphism through amphibolite-facies retrogression, as documented in UHP eclogite of the NEGEP (McClelland et al. 2006). Regression of ^{204}Pb-corrected core analyses, using the lower intercept age of 394 ± 12 Ma and rejecting one analysis due to assumed inheritance, gives an upper intercept of 2010 ± 10 Ma (MSWD = 1.4; Fig. 9a) which is the inferred age of the protolith.

A large leucotonalitic orthogneiss body near the SSZ extends as sills into grey biotite–amphibole tonalitic host gneiss. The tonalite and leucocratic gneiss are folded together by shallowly plunging isoclines. Sample 03-90 from a folded sill (Fig. 7b) contains about 63% feldspar, 20% quartz, 15% epidote group minerals, 1% biotite, 1% chlorite, and accessory zircon, apatite and opaque minerals. The rock has a protomylonitic foliation with coarse quartz ribbons alternating with fine-grained quartz + feldspar + epidote. Zircon from this sample is euhedral with oscillatory-zoned cores that are low in U, mantled by generally higher U zircon and by very thin, low U outer rims (Fig. 8b). The analyses are partly discordant and dispersed along concordia (Fig. 9b). Regression of 5 core analyses gives an upper intercept age of 1989 ± 13 Ma (MSWD = 1.6). Regression of 7 rims gives an upper intercept age of 1877 ± 10 Ma (MSWD = 1.4; Fig. 9b). Two analyses from the high U intermediate portions of the grains lie between these end member ages. The upper intercept ages determined from the core and rim analyses are interpreted as the time of emplacement and metamorphism of the orthogneiss protolith, respectively. Dispersion toward younger ages is attributed to Pb-loss during Caledonian metamorphism.

Pegmatite dikes locally cut the foliation in the leucotonalitic orthogneiss, and are themselves variably deformed. Sample 03-89 (Fig. 7c) is a cross-cutting pegmatite from the same locality as 03-90, and contains approximately 80% feldspar, 15% quartz, 2% biotite, 2% white mica 1% garnet, and trace amounts of epidote and chlorite. Euhedral, oscillatory-zoned zircon from the pegmatite (Fig. 8c) has relatively high U values of 217 to 3801 ppm, with no clear distinction between core and rim domains. The U–Pb analyses show considerable scatter, which we attribute to the combined effects of inheritance and metamorphism. Assuming a Caledonian lower intercept of ca. 395 Ma, regression through all but 2 analyses yields an upper intercept age of 1858 ± 9 Ma (MSWD = 3; Fig. 9c). This age is similar to the age of metamorphic zircon rims in the adjacent leucotonalitic orthogneiss and is interpreted as the

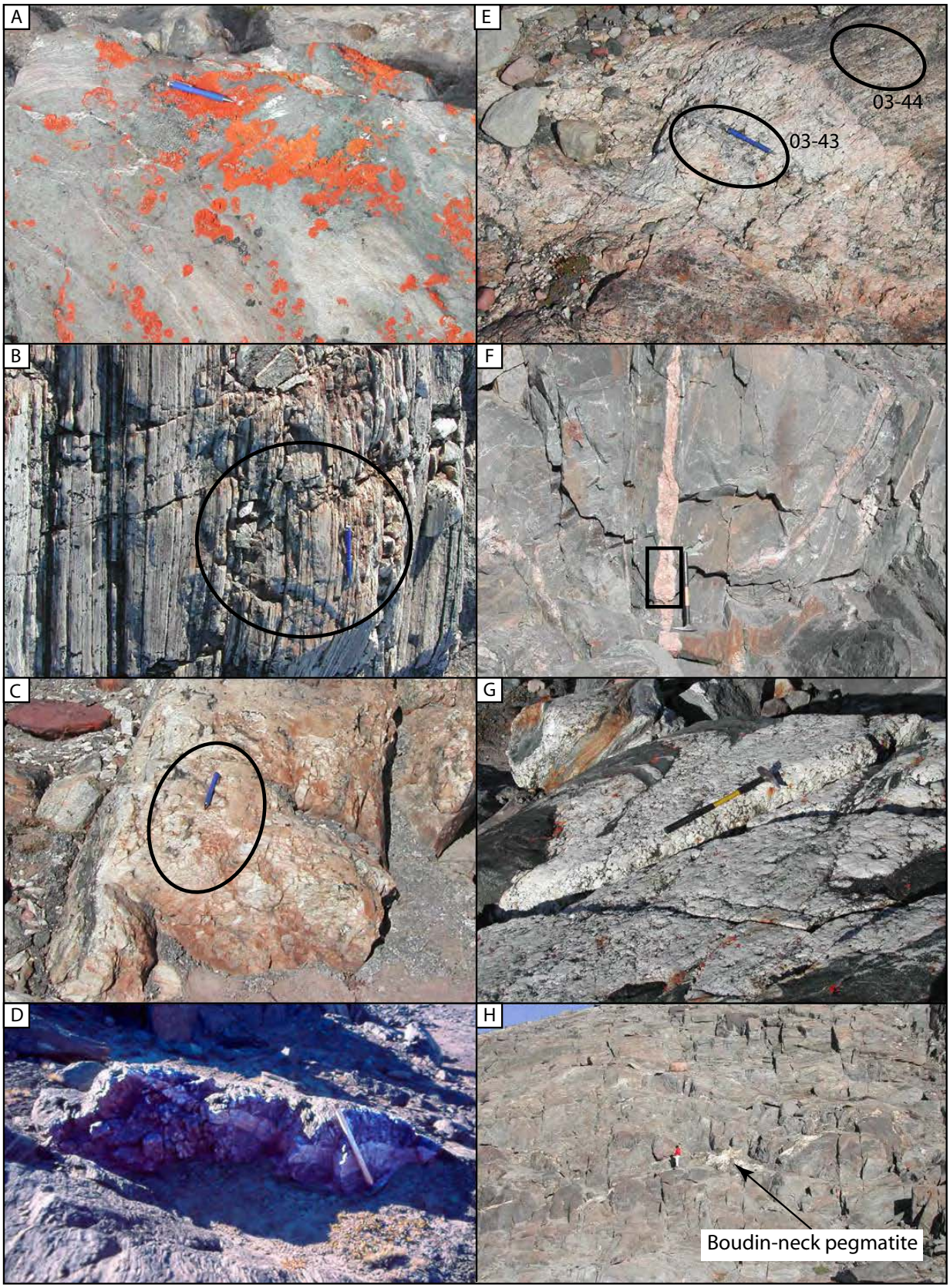

Figure 7. Outcrop photographs of U–Pb samples: (a) zoisite–kyanite eclogite 03-99 (ignore the orange lichen); (b) foliated leucotonalitic orthogneiss 03-90; (c) leucocratic pegmatite 03-89; (d) cross-cutting leucocratic dike 03-95 with subvertical gneissosity in the foreground; (e) pegmatite dike 03-43 cutting foliated metagranite 03-44 (note the different orientation of foliation in the metagranite fragment within the dike in lower left of photo); (f) pegmatite dike 03-40, within a sub-vertical mylonite zone; (g) coarse grained pegmatite 03-81 within boudin neck; (h) pegmatite 03-93 in boudin neck with a person for scale.

Table 1. Mineralogy and microstructures of dated samples from the Sanddal area.

U-Pb sample	Rock type	Qz	Fsp	Grt	Cpx	Amp	White mica	Bt	Chl	Ep Czo/Zo	Ttn	Zircon	Opaque minerals
03-38	augen mylonite	vfg-m	rx-pc, vfg-m				tr	vfg-m	tr	pc	fg-pc	a	a
03-39	mylonite	vfg-m	rx-pc, vfg-m	pc		pc		vfg-m		pc	fg-pc		a
03-40	pegmatite	c-rx, r	c-rx				s	tr			a	a	a
03-43	pegmatite	c-rx	c-rx				s	m	tr	m	m	a	
03-44	garnet-metagranite	c-rx, vfg-m	c-rx	pc		pc		m		1 pc, tr	a	a	
03-68	ultramylonite	vfg-m, r	rx-pc, vfg-m	pc			pc	vfg-m	tr	pc	fg-pc		a
03-76	granodioritic gneiss	c-r, vfg-m	c-rx, vfg-m	pc		pc		c&fg-m		m	m		a
03-81	boudin neck pegmatite		c-rx			c-n	s	m	m	m	m	a	
03-89	pegmatite	c-rx > vfg-m	c-rx > vfg-m	n		m	m, s	m	tr	tr		a	
03-90	mylonitic leucocratic orthogneiss	fg-m, r	fg-m					fg-m	fracs	fg-m		a	a
03-93	boudin neck pegmatite	c-rx	c-rx				m, s		tr	tr		a	
03-95	pegmatite	c-rx	c-rx	n			m, s		tr	tr		a	tr
03-99	retrogressed ky-eclogite	c-r	n	n	n, sym	n, m		tr		n		a +Rt	

Mineral Abbreviations after Whitney and Evans (2010); Fsp = feldspar; ky = kyanite. Other abbreviations are: c = coarse; fg = fine grained; vfg = very fine grained; a = accessory phase; n = neoblast; m = matrix; pc = porphyroclast; r = ribbon; rx = dynamically recrystallized, s = sericite; sym = symplectitic, tr = trace amounts.

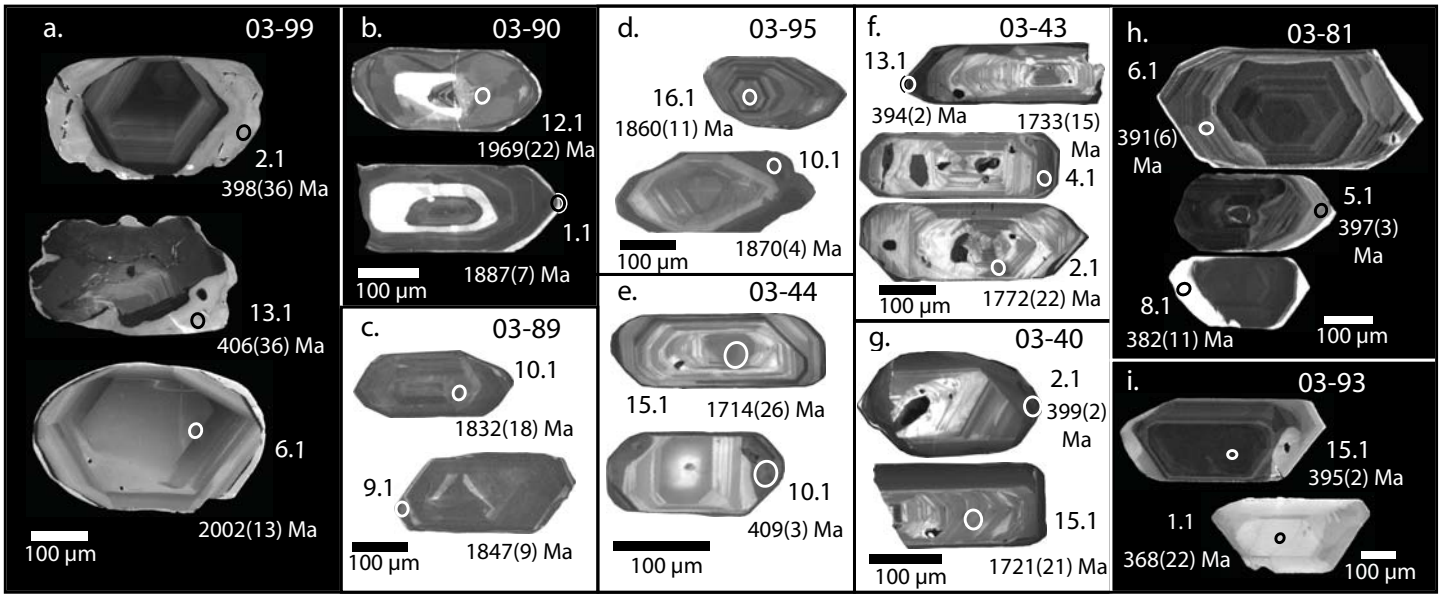

Figure 8. Representative cathodoluminescence (CL) images of zircon from (a) zoisite–kyanite eclogite 03-99; (b) foliated leucotonalitic orthogneiss 03-90; (c) leucocratic pegmatite 03-89; (d) leucocratic dike 03-95; (e) foliated metagranite 03-44; (f–g) pegmatite dikes, 03-43 and 03-40; (h–i) coarse grained pegmatites within boudin necks, 03-81 and 03-93. Ellipses indicate sensitive high-resolution ion microprobe–reverse geometry (SHRIMP–RG) analysis spots labeled by grain and spot number and the corresponding U–Pb ages (±1σ Ma).

approximate emplacement age of the pegmatite.

A similar pegmatite that cuts gneissic foliation in a granodioritic orthogneiss was sampled west of the leucotonalitic orthogneiss body. Sample 03-95 (Fig. 7d) consists of about 60% feldspar, 35% quartz, 5% white mica, with lesser amounts of garnet, epidote, zircon and opaque minerals. Elongate euhedral zircon contains cores (Fig. 8d) with moderate U (250–663 ppm) concentrations overgrown by higher U (1018–4417 ppm) rims. Regression of all but the four oldest core and one rim analyses with a fixed Caledonian lower intercept (ca. 395 Ma) yields an upper intercept age of 1876 ± 6 Ma (MSWD = 1.0; Fig. 9d), within error of the metamorphic zircon rim age in the leucocratic orthogneiss. Two possible interpretations are viable for this sample. A crystallization age of ca. 1875 Ma for the undeformed pegmatite dike suggests that much of the gneissic foliation in the Sanddal area is Precambrian in age. Alternatively, the observed ages may be derived from inherited zircon xenocrysts within a Caledonian pegmatite (see for example, Gilotti and McClelland 2005).

Sample 03-44 of foliated, garnet-bearing metagranite (Fig. 7e) from a large body in the centre of the field area consists of about 70% feldspar, 25% quartz, 4% biotite, 1% hornblende and accessory garnet, titanite, epidote, clinozoisite, apatite, and zircon. Zircon from the sample occurs as euhedral prisms with well-developed oscillatory zoning (Fig. 8e). Regression of all ^{204}Pb-corrected data gives an upper intercept age of 1751 ± 11 Ma (MSWD = 0.7), which is interpreted as the emplacement age (Fig. 9e). This body is distinctly younger than the leucotonalitic orthogneiss and pegmatites discussed above. Rim analyses from four grains give ^{207}Pb-corrected ^{206}Pb/^{238}U ages ranging from 409 to 457 Ma that, combined with the lower intercept age of 421 ± 14 Ma, indicates that some zircon rims grew in this unit during Caledonian metamorphism.

A trondhjemitic pegmatite (03-43) cross-cuts the metagranite, and was sampled near 03-44 (Fig. 7e). The pegmatite clearly cuts the penetrative foliation in the adjacent gneiss and contains blocky xenoliths of variably oriented granitic orthogneiss (Fig. 7e). The pegmatite is composed of about 93% feldspar, 5% quartz, 2% biotite and titanite, and accessory zircon. Deformation in this sample is expressed by dynamic recrystallization of feldspar to form subgrains. Elongate euhedral zircon shows oscillatory-

Figure 9. *(opposite and following pages)* Tera–Wasserburg U–Pb plots for zircon SHRIMP–RG analyses from (a) zoisite–kyanite eclogite 03-99; (b) foliated leucotonalitic orthogneiss 03-90; (c) leucocratic pegmatite 03-89; (d) leucocratic dike 03-95; (e) foliated metagranite 03-44; (f–g) pegmatite dikes, 03-43 and 03-40; (h–i) coarse grained pegmatites within boudin necks, 03-81 and 03-93. Ellipses plotted at 1σ. Proterozoic concordia intercept ages are calculated with ^{204}Pb corrected ratios. Paleozoic weighted mean ages are from ^{207}Pb-corrected ^{206}Pb/^{238}U ages (95% confidence level). MSWD = mean square of weighted deviates. Ellipses shown in light grey were excluded from age calculations (see text for discussion).

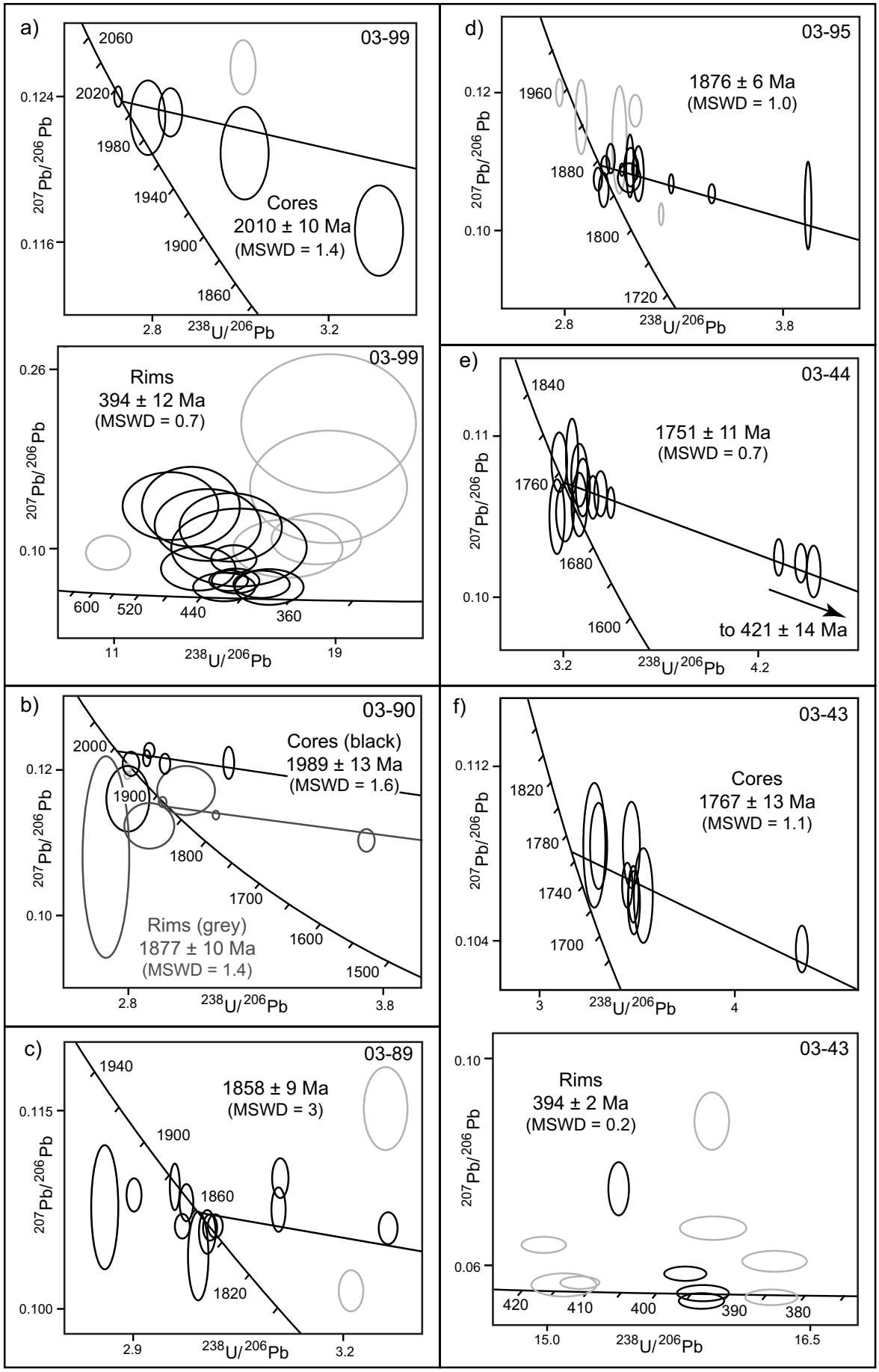
a)
03-99
Cores
2010 ± 10 Ma
(MSWD = 1.4)
Rims
394 ± 12 Ma
(MSWD = 0.7)
b)
03-90
Cores (black)
1989 ± 13 Ma
(MSWD = 1.6)
Rims (grey)
1877 ± 10 Ma
(MSWD = 1.4)
c)
03-89
1858 ± 9 Ma
(MSWD = 3)
d)
03-95
1876 ± 6 Ma
(MSWD = 1.0)
e)
03-44
1751 ± 11 Ma
(MSWD = 0.7)
to 421 ± 14 Ma
f)
03-43
Cores
1767 ± 13 Ma
(MSWD = 1.1)
03-43
Rims
394 ± 2 Ma
(MSWD = 0.2)
207Pb/206Pb
238U/206Pb

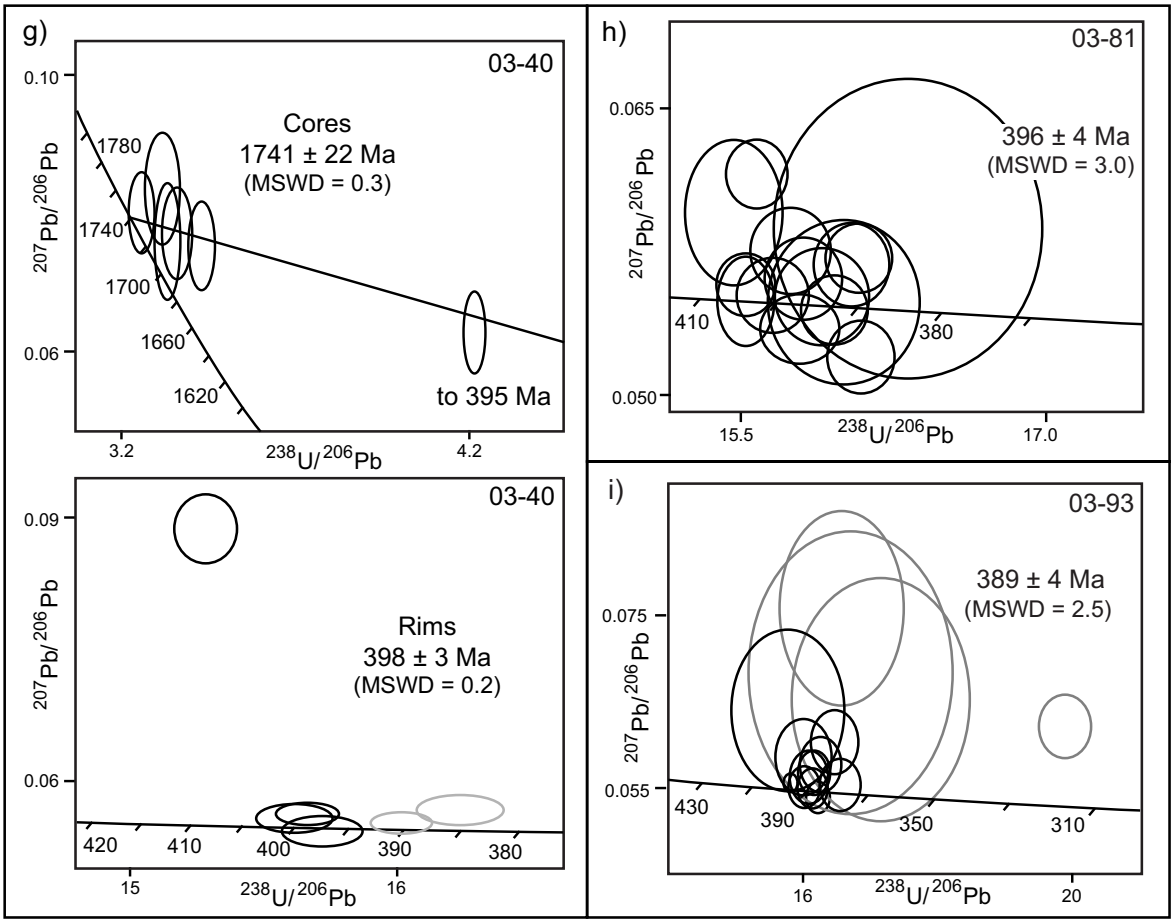

Figure 9. *(continued).*

zoned cores and well-developed, high U rims (Fig. 8f). The cores are clearly Proterozoic, whereas the rims yield both Proterozoic and Caledonian ages. Proterozoic cores and rims have U concentrations of 78–898 ppm and Th/U = 0.06–0.58. Caledonian rims have U concentrations of 255–2429 ppm and Th/U < 0.01. Regression of all ^{204}Pb-corrected data gives an upper intercept of 1767 ± 13 Ma (MSWD = 1.1; Fig. 9f). On the basis of age, compositional, and textural similarities, the older pegmatite zircon is interpreted as an inherited component derived from the adjacent granitic orthogneiss. The ^{207}Pb-corrected $^{206}Pb/^{238}U$ ages for low Th/U rims range from 376 to 413 Ma and yield a weighted mean age of 395 ± 8 Ma (MSWD = 26). Attributing the older ages to mixing between young rims and Proterozoic cores and the 4 younger analyses to retrograde growth and/or Pb-loss, the remaining analyses give a $^{206}Pb/^{238}U$ weighted mean age of 394 ± 2 Ma (MSWD = 0.2; Fig. 9f). A Caledonian emplacement age is plausible for the pegmatite based on the rim ages that are mainly younger than analyzed 03-44 rims, and field observation that the body cross-cuts and contains fragments of foliated metagranite (Fig. 7e).

A granitic pegmatite (03-40) within a 1metre-thick mylonite zone (Fig. 7f) that cuts the foliated metagranite (sample 03-44 above) is composed of approximately 90% feldspar, 10% quartz, and small amounts of biotite, apatite, zircon, titanite, and opaque minerals. Along its margin, the pegmatite has a weak mylonitic foliation defined by aligned biotite and quartz ribbons. Deformation of the pegmatite is recorded by embayed grain boundaries and dynamic recrystallization of feldspar. Elongate euhedral zircon has cores with Th/U ratios of 0.16 to 0.44 overgrown by 10 to 40 µm-thick rims with Th/U ratios of 0.002 to 0.11 (Fig. 8g). Regression of all analyses gives an upper intercept age of 1741 ± 22 Ma (MSWD = 0.3; Fig. 9g). The 10 rim ages range from 477 to 361 with 4 analyses having high common Pb. Assuming the oldest core age reflects a mixture of core and rim material, the 3 older ages from this sample give a weighted mean $^{206}Pb/^{238}U$ age of 398 ± 3 Ma (MSWD = 0.2; Fig. 9g), and thus a Caledonian emplacement age is interpreted for this pegmatite as well. The younger ages are interpreted to reflect continued new growth or Pb-loss after growth of new, low U rims at 398 ± 3 Ma.

Two pegmatite samples were collected from the necks of mafic boudins. Sample 03-81 was taken from the train of mafic pods extending south from the Sanddal mafic-ultramafic complex (Fig. 7g). The sample contains 70% sericitized feldspar and 20% green amphibole, which are overprinted by 6% chlorite intergrown with 1% biotite, 3% epidote and titanite. Other accessory minerals are apatite, titanite, and zircon. Euhedral zircon grains have small cores overgrown by oscillatory-zoned zircon (Fig. 8h) with moderate U (91 to 562 ppm), very low

Table 2. U–Pb SHRIMP zircon geochronologic data and apparent ages.

Spot†		U§ (ppm)	Th (ppm)	Th/U	$^{206}Pb^{*}$§ (ppm)	$f^{206}Pb_c$§	$^{238}U/^{206}Pb$#		$^{207}Pb/^{206}Pb$#		$^{206}Pb/^{238}U$†† (Ma)		$^{207}Pb/^{206}Pb$†† (Ma)	
Sample 03-99. Felsic eclogite (UTM 27 0492379; 8662613)														
1.1	c	204	71	0.36	58	1.6	3.006	(0.7)	0.1256	(0.8)	1825	(12)	2037	(14)
2.1	r**	2	0.03	0.02	0.1	8.2	14.419	(8.8)	0.1206	(17.5)	398	(36)		
3.1	r**	16	0.03	0.00	0.9	2.0	15.179	(3.0)	0.0710	(8.4)	403	(12)		
4.1	c*	71	13	0.19	20	0.9	3.012	(1.2)	0.1203	(1.4)	1833	(21)	1969	(25)
5.1	c*	110	21	0.20	34	0.2	2.791	(0.9)	0.1224	(1.1)	1971	(19)	1998	(20)
6.1	c*	267	55	0.21	81	0.5	2.842	(0.6)	0.1230	(0.7)	1935	(12)	2002	(13)
7.1	c*	2,960	272	0.09	934	-	2.723	(0.2)	0.1240	(0.3)	2017	(4)	2014	(5)
8.1	c*	89	21	0.25	23	1.7	3.309	(1.1)	0.1177	(1.4)	1677	(18)	1905	(26)
9.1	r	3	0.07	0.02	0.1	5.8	17.315	(7.6)	0.1002	(16.8)	341	(27)		
9.2	r	1	0.03	0.02	0.1	13	18.746	(10.0)	0.1548	(21.4)	293	(32)		
10.1	r**	3	0.18	0.07	0.2	8.0	15.240	(8.0)	0.1185	(17.0)	378	(31)		
11.1	r**	11	0.02	0.002	0.6	4.4	15.366	(3.5)	0.0902	(9.1)	389	(14)		
12.1	r**	6	0.02	0.004	0.4	1.3	15.018	(4.9)	0.0652	(12.9)	410	(20)		
13.1	r**	2	0.20	0.10	0.1	10	13.812	(8.5)	0.1370	(17.1)	406	(36)		
14.1	r**	2	0.02	0.01	0.1	10	13.068	(8.7)	0.1375	(14.5)	429	(38)		
15.1	r**	3	0.15	0.05	0.2	3.3	14.075	(6.3)	0.0819	(15.8)	428	(27)		
16.1	r	4	0.03	0.01	0.2	6.9	18.354	(5.9)	0.1083	(13.7)	319	(19)		
17.1	r**	6	0.04	0.01	0.3	1.4	16.652	(5.0)	0.0654	(16.1)	371	(19)		
18.1	r**	9	0.13	0.02	0.5	1.7	16.362	(4.2)	0.0678	(11.9)	376	(16)		
19.1	r	5	0.32	0.07	0.4	4.7	10.793	(5.0)	0.0969	(10.4)	545	(27)	2048	(135)
20.1	r	1	0.07	0.05	0.1	20	18.791	(11.1)	0.2116	(19.1)	269	(34)		
21.1	r**	10	0.19	0.02	0.6	2.0	15.433	(3.7)	0.0706	(10.1)	397	(15)		
22.1	r**	1	0.02	0.01	0.1	5.7	15.543	(10.4)	0.1004	(22.7)	380	(40)		
Sample 03-90. Leucocratic orthogneiss (UTM 27 0492112; 8660966)														
1.1	c*	504	7	0.01	147	0.8	2.942	(0.5)	0.12144	(0.7)	1874	(9)	1967	(14)
2.1	r**	361	16	0.05	114	-	2.713	(2.2)	0.10811	(8.5)	2060	(51)	1765	(156)
3.1	c*	23	0.1	0.00	7	-	2.793	(1.9)	0.11751	(2.4)	1981	(39)	1895	(46)
4.1	c*	783	328	0.43	234	0.5	2.872	(0.3)	0.12160	(0.6)	1918	(6)	1979	(11)
5.1	r**	551	97	0.18	156	0.6	3.027	(2.5)	0.11718	(1.9)	1831	(45)	1912	(35)
6.1	c*	375	12	0.03	112	0.7	2.882	(0.5)	0.12280	(0.6)	1909	(9)	1995	(10)
7.1	c*	154	23	0.16	47	0.0	2.810	(0.8)	0.12079	(0.9)	1961	(15)	1968	(16)
8.1	r	1,750	52	0.03	537	-	2.797	(0.3)	0.11921	(0.3)	1974	(5)	1944	(5)
9.1	r**	1,253	41	0.03	342	0.6	3.144	(0.3)	0.11373	(0.3)	1771	(5)	1859	(6)
10.1	r**	279	8	0.03	64	2.0	3.728	(0.6)	0.11107	(0.8)	1504	(8)	1802	(17)
11.1	r**	887	40	0.05	260	0.0	2.934	(0.3)	0.11566	(0.4)	1891	(6)	1887	(7)
12.1	c*	464	17	0.04	125	1.8	3.192	(0.4)	0.12121	(1.2)	1729	(8)	1969	(22)
13.1	r	1,011	29	0.03	311	-	2.796	(0.3)	0.12011	(0.4)	1973	(7)	1958	(6)
14.1	r**	1,316	64	0.05	392	-	2.881	(2.2)	0.11230	(1.8)	1932	(43)	1836	(34)
Sample 03-89. Pegmatite (UTM 27 0492112; 8660966)														
1.1	c*	1,654	184	0.1	457	0.7	3.108	(0.2)	0.11501	(0.4)	1788	(4)	1878	(8)
2.1	c	1,133	229	0.2	298	1.0	3.261	(0.3)	0.11305	(0.4)	1710	(5)	1848	(6)
3.1	c	217	50	0.2	57	1.6	3.254	(0.6)	0.11846	(0.8)	1703	(11)	1920	(16)
4.1	c*	2,005	291	0.2	571	0.04	3.017	(0.2)	0.11313	(0.3)	1845	(4)	1850	(5)
5.1	c*	2,443	308	0.1	676	0.5	3.105	(0.2)	0.11405	(0.5)	1792	(3)	1860	(9)
6.1	c*	2,096	289	0.1	607	-	2.969	(0.2)	0.11316	(0.3)	1874	(4)	1850	(5)
7.1	r*	1,465	181	0.1	434	-	2.902	(0.2)	0.11431	(0.4)	1914	(5)	1869	(6)
8.1	r*	754	57	0.08	202	0.5	3.209	(0.3)	0.11067	(0.5)	1742	(6)	1810	(8)
9.1	r*	1,255	41	0.03	359	0.02	3.004	(0.3)	0.11341	(0.5)	1852	(5)	1847	(9)
10.1	c*	841	104	0.1	241	-	2.992	(0.3)	0.11224	(1.0)	1862	(6)	1832	(18)
11.1	r*	1,801	220	0.1	514	0.01	3.009	(0.2)	0.11313	(0.3)	1850	(4)	1849	(5)
12.1	c*	1,814	274	0.2	524	-	2.976	(0.2)	0.11404	(0.4)	1868	(4)	1864	(7)
13.1	c*	629	82	0.1	189	-	2.859	(0.4)	0.11398	(1.4)	1943	(9)	1861	(25)

(continued)

Table 2. U–Pb SHRIMP zircon geochronologic data and apparent ages *(continued)*.

Spot†		U§ (ppm)	Th (ppm)	Th/U	$^{206}Pb^{*}$§ (ppm)	$f^{206}Pb_c$§	$^{238}U/^{206}Pb$#		$^{207}Pb/^{206}Pb$#		$^{206}Pb/^{238}U$†† (Ma)		$^{207}Pb/^{206}Pb$†† (Ma)	
Sample 03-89. Continued														
14.1	c*	3,801	762	0.2	1104	-	2.959	(0.2)	0.11455	(0.5)	1877	(3)	1873	(9)
Sample 03-95. Pegmatite (UTM 27 0492379; 8662613)														
1.1	c*	663	207	0.3	182	0.6	3.124	(0.4)	0.11441	(0.5)	1780	(6)	1871	(8)
2.1	c	439	155	0.4	127	-	2.980	(0.5)	0.11316	(0.7)	1867	(10)	1847	(13)
3.1	c	464	239	0.5	143	-	2.780	(0.4)	0.12007	(0.5)	1985	(9)	1955	(10)
4.1	c	614	300	0.5	176	0.1	2.990	(0.4)	0.11453	(0.5)	1858	(7)	1873	(8)
5.1	c*	595	226	0.4	173	-	2.956	(0.4)	0.11371	(0.5)	1881	(8)	1859	(9)
6.1	r*	4,417	733	0.2	1158	1.3	3.278	(0.2)	0.11558	(0.4)	1696	(3)	1853	(7)
7.1	c*	440	324	0.8	121	1.3	3.123	(0.6)	0.11927	(0.6)	1771	(10)	1936	(11)
8.1	r*	2,186	423	0.2	516	9.2	3.643	(0.3)	0.16882	(0.9)	1435	(5)	1827	(34)
9.1	c	250	82	0.3	70	0.8	3.049	(0.7)	0.11774	(2.1)	1816	(14)	1902	(40)
10.1	r*	3,098	96	0.0	868	0.4	3.066	(0.2)	0.11436	(0.2)	1814	(3)	1870	(4)
11.1	c*	337	123	0.4	92	0.7	3.137	(0.5)	0.11431	(1.1)	1773	(9)	1865	(20)
12.1	c	266	109	0.4	74	0.6	3.100	(0.6)	0.11514	(0.8)	1792	(11)	1872	(15)
13.1	r*	1,646	123	0.1	469	3.4	3.012	(0.3)	0.13940	(0.9)	1793	(6)	1874	(24)
14.1	c*	373	105	0.3	111	0.1	2.876	(0.6)	0.11881	(1.5)	1921	(12)	1929	(27)
15.1	r*	1,018	377	0.4	252	1.6	3.472	(0.3)	0.11267	(0.4)	1609	(5)	1841	(7)
16.1	c*	433	148	0.4	120	0.5	3.097	(1.1)	0.11376	(0.6)	1797	(19)	1860	(11)
17.1	r*	2,876	426	0.2	765	1.0	3.230	(0.2)	0.11425	(0.3)	1723	(4)	1818	(8)
18.1	c*	426	136	0.3	121	0.3	3.011	(0.5)	0.11541	(0.6)	1843	(9)	1882	(11)
Sample 03-44. Metagranite (UTM 27 0486847; 8664100)														
1.1	r*	507	58	0.12	99	2.2	4.415	(0.4)	0.10276	(0.7)	1290	(5)	1663	(14)
2.1	r*	358	1	0.004	23	1.2	13.453	(0.6)	0.06565	(1.7)	457	(3)		
3.1	r*	663	95	0.15	132	2.1	4.300	(0.4)	0.10349	(0.6)	1322	(5)	1669	(13)
4.1	r*	338	67	0.2	65	2.3	4.475	(0.5)	0.10304	(0.8)	1273	(6)	1654	(19)
5.1	r*	399	3	0.01	25	0.9	13.603	(0.6)	0.06307	(1.7)	453	(3)		
6.1	r*	166	1	0.005	11	12.3	13.144	(0.9)	0.15450	(3.3)	416	(5)		
7.1	r*	311	9	0.03	30	2.6	8.804	(0.6)	0.08356	(1.3)	676	(4)	1257	(29)
8.1	c*	214	81	0.4	54	0.6	3.395	(0.6)	0.10666	(0.9)	1656	(10)	1739	(16)
9.1	c*	127	81	0.7	34	0.1	3.183	(0.8)	0.10865	(1.1)	1759	(14)	1772	(21)
10.1	r*	357	1	0.004	20	0.2	15.237	(0.6)	0.05638	(1.9)	409	(3)		
11.1	r*	664	138	0.2	166	0.8	3.444	(0.4)	0.10701	(0.5)	1632	(6)	1729	(11)
12.1	c*	156	61	0.4	41	0.4	3.302	(0.7)	0.10779	(1.0)	1699	(12)	1745	(20)
13.1	c*	237	124	0.5	63	0.9	3.231	(0.6)	0.11370	(1.0)	1724	(10)	1778	(25)
14.1	c*	128	82	0.7	34	-	3.212	(0.9)	0.10575	(1.1)	1749	(16)	1719	(20)
15.1	c*	124	74	0.6	33	-	3.172	(0.8)	0.10550	(1.4)	1772	(14)	1714	(26)
16.1	c*	111	41	0.4	29	0.3	3.288	(0.9)	0.10720	(1.2)	1707	(15)	1758	(22)
17.1	c*	118	48	0.4	31	0.2	3.282	(0.8)	0.10669	(1.1)	1711	(14)	1727	(22)
18.1	c*	242	89	0.4	62	0.4	3.354	(0.6)	0.10649	(0.8)	1676	(9)	1735	(15)
Sample 03-43. Pegmatite cross-cutting metagranite (UTM 27 0486843; 8664106)														
1.1	r*	470	80	0.2	93	2.2	4.338	(0.4)	0.10366	(0.7)	1310	(6)	1690	(13)
2.1	c*	110	62	0.6	29	0.5	3.305	(0.9)	0.10834	(1.2)	1697	(15)	1772	(22)
4.1	c*	315	85	0.3	78	0.8	3.481	(0.5)	0.10677	(0.8)	1616	(9)	1733	(15)
5.1	c*	119	51	0.4	29	1.0	3.473	(0.9)	0.10839	(1.2)	1617	(14)	1772	(22)
6.1	c*	78	5	0.06	8	2.5	8.358	(1.3)	0.08402	(2.7)	711	(9)	1148	(96)
7.1	r*	898	58	0.07	106	4.6	7.252	(0.4)	0.10375	(0.7)	797	(3)	1435	(29)
8.1	c*	299	86	0.3	74	0.8	3.483	(0.6)	0.10667	(0.8)	1615	(9)	1727	(17)
9.1	c*	81	31	0.4	21	0.7	3.272	(1.1)	0.11099	(1.5)	1708	(18)	1772	(32)
10.1	c*	111	52	0.5	27	0.9	3.532	(1.0)	0.10603	(1.3)	1595	(15)	1732	(25)
11.1	c*	432	105	0.3	108	0.7	3.450	(0.5)	0.10665	(0.6)	1630	(7)	1741	(12)
12.1	r*	431	2	0.004	23	-	16.284	(0.6)	0.05388	(1.9)	384	(2)		

(continued)

Table 2. U–Pb SHRIMP zircon geochronologic data and apparent ages *(continued)*.

Spot†		U§ (ppm)	Th (ppm)	Th/U	$^{206}Pb^{*}$§ (ppm)	$f^{206}Pb_c$§	$^{238}U/^{206}Pb$#		$^{207}Pb/^{206}Pb$#		$^{206}Pb/^{238}U$†† (Ma)		$^{207}Pb/^{206}Pb$†† (Ma)	
Sample 03-43. Continued														
13.1	r**	623	3	0.004	34	0.5	15.788	(0.5)	0.05840	(1.5)	394	(2)		
14.1	r**	2,429	7	0.003	135	2.5	15.408	(0.3)	0.07494	(4.5)	395	(2)		
15.1	r*	503	23	0.05	29	1.1	14.982	(0.6)	0.06401	(1.7)	412	(2)		
16.1	r*	308	1	0.003	16	0.8	16.302	(0.8)	0.06083	(2.2)	381	(3)		
17.1	r*	713	2	0.003	40	0.2	15.188	(0.5)	0.05671	(1.4)	410	(2)		
18.1	r*	255	1	0.003	15	0.2	15.095	(0.8)	0.05627	(2.6)	413	(3)		
19.1	r**	413	1	0.004	22	0.0	15.891	(0.6)	0.05472	(1.9)	393	(2)		
Sample 03-40. Pegmatite (UTM 27 0487195; 8665209)														
1.1	c*	550	86	0.2	112	1.9	4.207	(0.5)	0.10253	(1.0)	1352	(7)	1658	(20)
2.1	r**	418	1	0.002	23	0.1	15.622	(0.6)	0.05571	(1.8)	399	(2)		
3.1	r*	419	8	0.02	22	0.3	16.249	(0.7)	0.05674	(2.1)	384	(3)		
4.1	r**	388	1	0.002	21	0.0	15.728	(0.6)	0.05434	(2.1)	398	(3)		
5.1	r**	581	2	0.003	32	0.2	15.670	(0.5)	0.05629	(1.5)	398	(2)		
6.1	r*	661	1	0.002	35	0.1	16.026	(0.5)	0.05525	(1.4)	390	(2)		
7.1	r*	687	30	0.04	45	19.2	13.012	(0.5)	0.20962	(1.6)	388	(3)		
8.1	r*	484	49	0.11	26	9.1	15.805	(0.5)	0.12707	(7.3)	361	(5)		
9.1	r*	652	16	0.03	47	8.2	11.950	(0.5)	0.12308	(9.7)	477	(8)		
10.1	r*	621	16	0.03	35	4.2	15.289	(0.5)	0.08875	(2.9)	392	(2)		
11.1	c*	145	57	0.4	37	0.4	3.328	(0.8)	0.10674	(1.4)	1688	(13)	1725	(28)
12.1	c*	160	61	0.4	42	0.2	3.256	(0.7)	0.10739	(1.0)	1723	(12)	1745	(19)
13.1	c*	86	37	0.4	22	0.5	3.318	(1.0)	0.10825	(1.4)	1690	(17)	1762	(26)
14.1	c*	161	57	0.4	41	0.4	3.361	(0.9)	0.10592	(1.2)	1674	(14)	1730	(21)
15.1	c*	164	65	0.4	41	0.6	3.427	(0.7)	0.10624	(1.0)	1642	(12)	1721	(21)
20.1	r*	257	2	0.009	14	1.6	15.948	(0.8)	0.06718	(2.2)	386	(3)		
21.1	r**	529	2	0.003	29	-	15.882	(0.5)	0.05315	(1.8)	394	(2)		
22.1	r*	931	2	0.003	50	4.2	15.941	(0.4)	0.08778	(4.2)	376	(2)		
Sample 03-81. Pegmatite in boudin neck (UTM 27 0484416; 8666530)														
1.1	c*	364	0.5	0.001	20	0.2	15.768	(0.8)	0.0560	(2.5)	396	(3)		
2.1	c*	224	0.2	0.001	12	0.1	15.862	(1.0)	0.0551	(3.1)	394	(4)		
3.1	c*	361	1.0	0.003	19	0.3	16.012	(0.8)	0.0568	(2.5)	389	(3)		
4.1	c*	440	1.2	0.003	24	0.3	16.051	(0.7)	0.0571	(2.1)	388	(3)		
5.1	c*	444	8.2	0.019	24	-	15.748	(0.8)	0.0534	(2.2)	397	(3)		
6.1	r*	91	0.2	0.002	5	0.05	15.975	(1.6)	0.0549	(5.1)	391	(6)		
7.1	c*	394	0.6	0.002	21	-	15.925	(0.7)	0.0543	(2.2)	393	(3)		
8.1	r	28	0.0	0.002	2	0.5	16.302	(2.8)	0.0586	(8.7)	382	(11)		
9.1	c*	545	1.0	0.002	30	0.8	15.527	(0.7)	0.0614	(1.9)	399	(3)		
10.1	c	404	47.3	0.121	95	2.1	3.666	(0.6)	0.1131	(0.8)	1526	(9)	1829	(16)
11.1	c*	562	0.8	0.001	30	-	16.056	(0.7)	0.0520	(2.3)	391	(3)		
12.1	c*	220	1.2	0.006	12	0.6	15.410	(1.1)	0.0594	(4.1)	403	(4)		
13.1	c*	276	7.1	0.027	15	0.3	15.703	(0.9)	0.0574	(2.5)	397	(3)		
14.1	c*	463	1.1	0.002	26	0.1	15.472	(0.6)	0.0557	(1.9)	403	(3)		
15.1	c*	324	2.3	0.007	18	0.1	15.610	(0.8)	0.0552	(2.3)	400	(3)		
16.1	c*	490	0.6	0.001	27	0.01	15.472	(0.6)	0.0549	(2.7)	404	(3)		
Sample 03-93. Pegmatite in boudin neck (UTM 27 0491103; 8662225)														
1.1	c	7	0.02	0.004	0	1.8	16.699	(6.0)	0.0682	(15.8)	368	(22)		
2.1	c	8	0.02	0.002	0	1.4	17.161	(5.1)	0.0651	(14.3)	360	(18)		
3.1	c	183	11.8	0.067	8	1.2	19.883	(1.2)	0.0619	(3.9)	313	(4)		
4.1	c	118	0.5	0.004	6	0.7	16.461	(1.4)	0.0602	(4.1)	377	(5)		
5.1	c*	252	0.03	0.0001	14	0.1	16.011	(1.0)	0.0550	(2.9)	390	(4)		
6.1	c	189	2.8	0.015	10	0.1	16.545	(1.2)	0.0552	(3.6)	378	(5)		
7.1	c*	250	0.04	0.0001	13	0.3	16.156	(1.0)	0.0566	(3.0)	386	(4)		

(continued)

Table 2. U–Pb SHRIMP zircon geochronologic data and apparent ages *(continued)*.

Spot†		U§ (ppm)	Th (ppm)	Th/U	$^{206}Pb^{*}$§ (ppm)	$f^{206}Pb_c$§	$^{238}U/^{206}Pb$#		$^{207}Pb/^{206}Pb$#		$^{206}Pb/^{238}U$†† (Ma)		$^{207}Pb/^{206}Pb$†† (Ma)
Sample 03-93. Continued													
8.1	r*	63	0.02	0.0003	3	0.5	16.001	(1.7)	0.0584	(5.0)	389	(7)	
9.1	c*	276	0.05	0.0002	15	0.1	16.134	(0.9)	0.0548	(2.8)	387	(4)	
10.1	r*	17	0.02	0.001	1	1.2	15.768	(3.5)	0.0638	(9.6)	392	(14)	
11.1	c*	149	0.06	0.0004	8	0.2	16.098	(1.2)	0.0561	(3.6)	388	(5)	
12.1	c*	321	0.06	0.0002	17	-	16.215	(0.7)	0.0538	(2.2)	386	(3)	
13.1	c	15	0.02	0.002	1	2.7	16.565	(3.7)	0.0756	(9.8)	368	(14)	
14.1	r*	115	0.04	0.0003	6	0.4	16.253	(1.3)	0.0576	(3.7)	383	(5)	
15.1	c*	949	0.6	0.001	52	0.1	15.826	(0.4)	0.0555	(1.3)	395	(2)	

Note: All analyses were performed on the SHRIMP–RG (sensitive high mass resolution ion microprobe – reverse geometry) ion microprobe at the United States Geological Survey–Stanford analytical facility, Stanford, CA.

† Spots reported as grain number-analysis number. c =core; r = rim. Annotations indicate analyses used in first (*) and second (**) age calculations.

§ Pb* denotes radiogenic Pb; Pb_c denotes common Pb; $f^{206}Pb_c = 100*(^{206}Pb_c/^{206}Pb_{total})$

Reported ratios are not corrected for common Pb. Errors are reported in parentheses as percent at the 1 σ level.

†† Ages calculated from ratios corrected for common Pb using ^{207}Pb-method for the $^{206}Pb/^{238}U$ age and ^{204}Pb-method for the $^{207}Pb/^{206}Pb$ age. Uncertainties in millions of years reported as 1 σ.

Th (0.2–8.2) and Th/U (0.001–0.03), and $^{206}Pb/^{238}U$ ages ranging from 388 to 404 Ma (Fig. 9h). A discordant analysis from a core indicates the presence of Proterozoic inherited components. Most grains have very thin (1–5 μm), low U rims (Fig. 8h). A single analysis of a low U rim gives a distinctly younger age. The remaining analyses yield a weighted mean age of 396 ± 4 Ma (MSWD = 3.1). There is a general decrease in both U and Th with decreasing age, suggesting that the age spread could possibly be due to continued zircon growth between approximately 403 and 390 Ma. Attributing younger ages to overgrowth and/or Pb-loss, the 8 oldest ages give a weighted mean age of 400 ± 3 Ma (MSWD = 1.1; Fig. 9h), which may record the time of initial emplacement for this sample. However, distinguishing between Pb-loss and/or continuous or multiple zircon growth events is not possible based on chemistry or textural arguments.

The second boudin neck pegmatite (03-93, Fig. 7h), located just west of the SSZ, is composed of approximately 90% feldspar, 8% quartz, and 2% white mica, chlorite and epidote. Zircon is the important accessory phase. Chlorite and epidote replace white mica, and the feldspar is sericitized. Zircon is euhedral and consists of grains with oscillatory-zoned higher U cores overgrown by lower U rims or homogeneous low U grains (Fig. 8i). Excluding the youngest analysis, which is clearly anomalous, and the core analyses from low U grains, regression of the remaining 11 analyses yields a weighted mean age of 389 ± 4 Ma (MSWD = 2.5; Fig. 9i), the inferred emplacement age for the pegmatite. The younger analyses are interpreted to record continued (re)crystallization and/or Pb-loss.

Interpretation

U–Pb zircon geochronology reported above suggests zircon growth occurred during Proterozoic plutonism and metamorphism, followed by renewed tectonism that involved regional HP metamorphism, subsequent retrograde metamorphism, and pegmatite intrusion in the Devonian. The lack of Caledonian rims on most zircon grains from the Paleoproterozoic orthogneiss and pegmatites indicate that quartzofeldspathic protoliths were not conducive to new zircon growth during Caledonian metamorphism. Similar relations are observed elsewhere in the NEGEP (e.g. Kalsbeek et al. 1999). Nevertheless, the presence of small Paleozoic pegmatites indicates that localized melting occurred during Caledonian metamorphism and deformation.

Proterozoic U–Pb zircon ages range from 2010 ± 10 Ma for felsic eclogite to 1755 ± 11 Ma for garnet metagranite (Fig. 10). The eclogite protolith from this study is older than the protolith age of 1962 ± 27 Ma determined for a leucogabbro west of the SSZ (Gilotti et al. 2004) and suggests that the mafic rocks may in part be screens in the younger calc-alkaline arc complex. The leucotonalite intrusion (03-90) at ~1.99 Ga falls in the older age range of the Paleoproterozoic calc-alkaline suite. Metamorphism and pegmatite emplacement at ca. 1870 Ma and granite emplacement at 1755 Ma provide additional documentation for a complex thermal and magmatic history (Kalsbeek et al. 2008). The truncation of older fabrics by younger Paleoproterozoic igneous units also supports regional observations for an early deformational history (Hull et al. 1994).

Paleozoic ages from zircon rims and pegmatites range from 402 ± 13 Ma to 390 ± 4 Ma. The zircon rim age from the felsic zoisite + kyanite eclogite (402 ± 13 Ma) is in agreement with zircon ages of 414 ± 13, 401 ± 7 and 394 ± 10 Ma and Sm–Nd isochron ages of 401 ± 2, 402 ± 9 and 414 ± 18 Ma reported from eclogite elsewhere in the western block (Gilotti et al. 2004). On the basis of zircon geochemistry, these ages are interpreted to represent HP metamorphism of the western

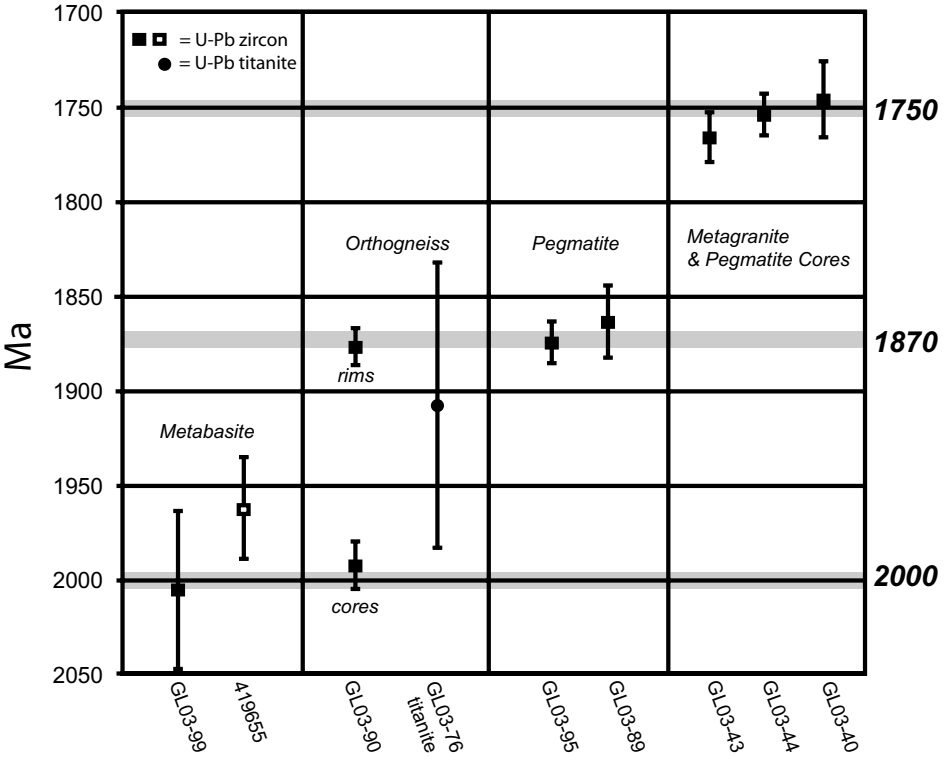

Figure 10. Summary diagram of Precambrian U–Pb zircon and titanite ages from Sanddal. Solid symbols = this study, open symbols = Gilotti et al. (2004). Grey bands approximate major zircon and titanite growth events.

block of the NEGEP at approximately 415–395 Ma (Gilotti et al. 2004). The boudin neck pegmatites were emplaced during amphibolite-facies metamorphism since both the pegmatites and deformation fabrics along the eclogite margins involve retrograde minerals (e.g. Sartini-Rideout et al. 2006, 2009). All of the Caledonian pegmatite samples are interpreted to reflect decompression and retrograde amphibolite-facies metamorphism of the western block between 395 and 390 Ma. Since there is no direct tie between zircon growth and *P-T* conditions for these samples, the older age of 400 ± 3 Ma may record initial zircon growth during pegmatite emplacement at eclogite-facies conditions.

Titanite U–Pb Geochronology

U–Pb titanite (SHRIMP) ages were obtained to estimate the timing of amphibolite-facies metamorphism preserved in the metamorphic rocks outside of the SSZ and the age of deformation within the SSZ. Titanite was separated from granodioritic orthogneiss (03-76), a boudin neck pegmatite (03-81), mylonitic garnet-bearing metagranite from west of the SSZ (03-39), and two mylonite samples (03-38 and 03-68) from the SSZ proper (Fig. 2). Figure 11 presents backscattered electron (BSE) images of representative titanite grains. Table 3 contains the U–Pb geochronologic data and ages, which are plotted in Tera–Wasserburg diagrams in Figure 12.

Sample Description and Results

Granodioritic orthogneiss sample 03-76, collected approximately 7 km west of the SSZ, consists of 39% alkali feldspar, 25% quartz, 20% plagioclase, 15% biotite, and 1% amphibole, garnet, and epidote-group minerals. Accessory minerals are apatite, titanite, zircon and opaque minerals. Compositional banding between biotite-rich and quartzofeldspathic layers, parallel alignment of biotite grains, and ribbons of coarse-grained quartz define the gneissic fabric. Microstructures, such as recrystallization around large porphyroclasts, are symmetrical. Titanite varies from rhomb-shaped to anhedral fragments and occurs as either brown or clear grains. Grains of both colour varieties are aligned with their long axes parallel to the foliation. Brown grains have well defined cores and distinct rims (Fig. 11a); the rims are similar to the uniform, colourless grains. Many cores are cut by internal vein networks that look like the rim material in BSE and are inferred to record partial replacement or recrystallization of the cores during rim growth. The cores are compositionally distinct with higher U (70–285 ppm), Th (37–111 ppm), and Th/U (0.4–1.3) than the rims and clear grains (U = 5–201 ppm; Th = 0.1–6.2; Th/U = 0.03–0.06). Discordant core analyses are interpreted to reflect Proterozoic and Caledonian components and common Pb (Fig. 12a). A 3-dimensional planar regression yields an upper intercept age of 1894 ± 78 Ma (MSWD = 0.5). Analyses of the rims and clear grains define a linear array between common Pb and metamorphic titanite formed at 353 ± 13 Ma (MSWD = 2.4).

Titanite from a boudin neck pegmatite sample 03-81 (see description of zircon sample) occurs as anhedral to subhedral matrix grains with faint core to rim zoning observed in BSE images (Fig. 11b). The grains have low U and Th concentrations and Th/U with no substantial core to rim variation. Regression of all analyses save one that falls off of the linear array (Fig. 12b) gives an age of 352 ± 12 (MSWD = 1.8).

A mylonite (03-39) derived from garnet metagranitoid rock was collected from the same 1 m thick shear zone that contains the pegmatitic granite 03-40 (Fig. 11d). The sample contains approximately 35% alkali feldspar, 30% quartz, 20% plagioclase, 12% biotite, 3% hornblende, and small amounts of garnet + epidote group minerals. Titanite and opaque minerals are common accessory minerals. Fine-grained biotite defines a mylonitic fabric and weak shear bands that indicate a sinistral shear sense. Rounded epidote and titanite occur in biotite-rich bands, often as overgrowths on hornblende porphyroclasts. Clear titanite has faint, gradational core to rim zoning (Fig. 12c), with a general core to rim increase in U and Th concentrations and Th/U. Regression of all analyses yields an age of 355 ± 8 Ma (MSWD = 2.3).

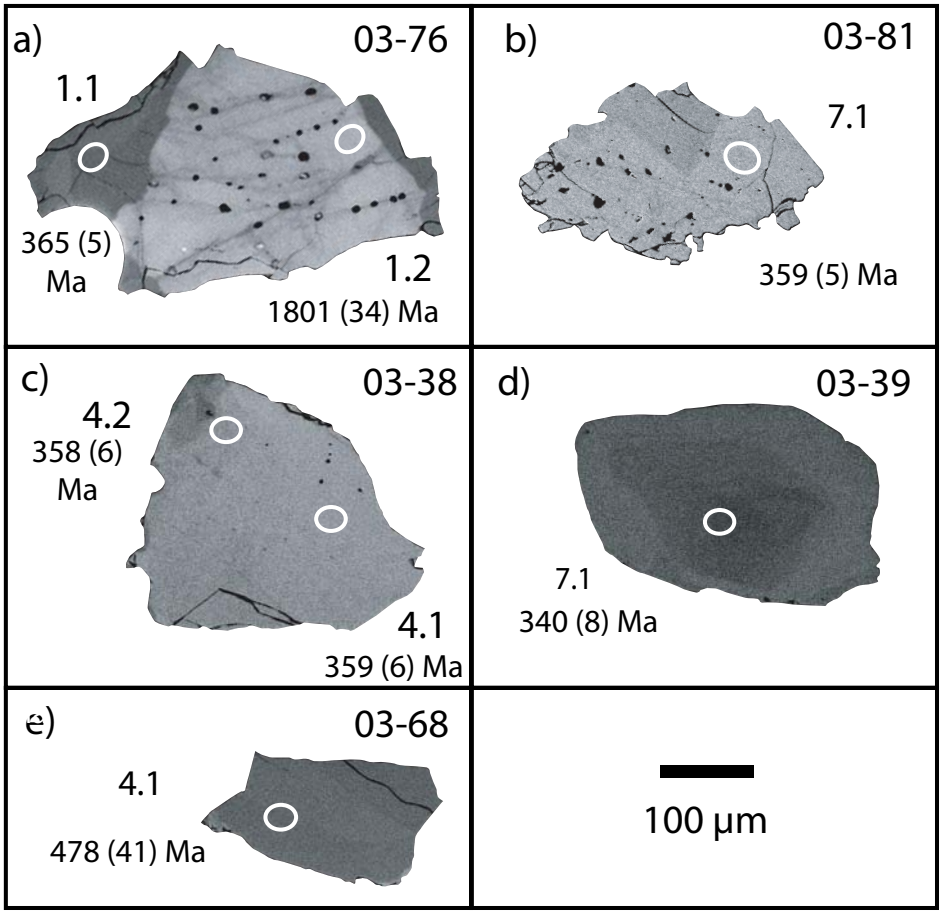

Figure 11. Representative backscattered electron images of titanite. Circles indicate SHRIMP analysis locations and corresponding U–Pb ages (± 1σ). Spot numbers marked as grain number and analysis number. (a) Subangular brown titanite from 03-76 has bright cores and darker rims. (b) Angular titanite fragment with multiple inclusions and patchy zoning, 03-81. (c) Subrounded titanite from mylonite 03-38 showing some patchy zoning. (d) Subrounded titanite with an intermediate rim grading to a slightly darker core, mylonite 03-39. (e) Anhedral, subrounded titanite with relatively flat zoning profile from ultramylonite 03-68.

Augen mylonite 03-38, from near the western edge of the SSZ, is composed of 40% plagioclase, 20% quartz, 20% alkali feldspar, 15% biotite, 5% epidote group, and accessory titanite, chlorite, apatite, white mica, and opaque minerals. Partially altered feldspar porphyroclasts with abundant mechanical twinning show white mica-filled fractures and recrystallized tails that indicate sinistral displacement. Brown and clear titanite porphyroclasts in the quartz + feldspar + biotite matrix have long axes parallel to the mylonitic foliation. Brown titanite typically has higher U cores rimmed by low U material that is similar in appearance and U, Th, and Th/U to clear titanite (Fig. 11c). Regression of all but two analyses gives a lower intercept of 354 ± 5 Ma (MSWD = 0.4). The two core analyses that fall off the linear regression are interpreted to reflect relict Proterozoic titanite (Fig. 12d).

Ultramylonite 03-68 from the SSZ contains approximately 40% biotite, 33% feldspar, 25% quartz, 1% garnet, 1% epidote group minerals, together with accessory titanite, white mica, apatite, and zircon. Titanite forms subhedral to anhedral grains in the matrix, as well as small fish between biotite shear bands (see example in Fig 6b). In BSE images (Fig. 11e), titanite is relatively dark and fairly patchy. Extremely low U, Th, and Pb concentrations prevented analysis of this sample; however, the one successful spot is consistent with the relatively high common Pb analyses from the other samples.

Interpretation

Titanite from the orthogneiss distal to the SSZ at Sanddal has seen two growth episodes. The angular cores record either primary igneous crystallization (e.g. Aleinikoff et al. 2002) or metamorphism in the Paleoproterozoic. Clear rims and grains grew during a late-stage regional fluid event that may be related to continued exhumation during shearing along the SSZ and related minor shear zones.

U–Pb titanite ages from mylonite indicate that titanite growth continued after all documented zircon growth at Sanddal. This growth is interpreted to record a fluid flux associated with formation of mylonite and ultramylonite within the SSZ and related smaller shear zones at greenschist-facies conditions. Deformed porphyroclasts of titanite in mylonite (Fig. 6b) indicate that deformation continued after these grains crystallized. The extremely low U concentrations in titanite from ultramylonite (GL03-68; Table 3) are interpreted to reflect continued titanite crystallization from a very low U fluid. This low U event is not recognized in other U–Pb samples and may be concentrated in the youngest portions of the SSZ. The SSZ was active during and following titanite growth at 350 Ma, i.e. it was still an active structure well into the Carboniferous.

DISCUSSION AND CONCLUSIONS

The new mapping and age data presented above support an interpretation that the SSZ is part of an array of conjugate sinistral and dextral faults that formed late in the Caledonian collision. The SSZ consists of anastomosing 100 m thick mylonite to ultramylonite zones superimposed on quartzofeldspathic gneiss and eclogite that have compound fabrics resulting from superposed Paleoproterozoic and Caledonian deformation (Fig. 2).

Timing of Strike-Slip Deformation Along the SSZ

Zircon ages from eclogite and pegmatites indicate Paleoproterozoic deformation followed by granite emplacement at ca. 1.75 Ga and HP metamorphism at ca. 400 Ma followed

Table 3. U–Pb SHRIMP titanite geochronologic data and apparent ages.

Spot†		U§ (ppm)	Th (ppm)	Th/U	$^{206}Pb^{*}$§ (ppm)	$f^{206}Pb_c$§	$^{206}Pb/^{204}Pb$§		$^{238}U/^{206}Pb$#		$^{207}Pb/^{206}Pb$#		$^{206}Pb/^{238}U$†† (Ma)	
Sample 03-76. Quartzofeldspathic orthogneiss (UTM 27 048445; 8662950)														
1.1	r*	128	6.2	0.05	7.3	12	177	(18)	15.059	(1.2)	0.15284	(1.2)	365	(5)
1.2	c**	219	147	0.70	41.7	4	1410	(14)	4.503	(1.1)	0.11976	(1.2)	1240	(13)
2.1	r*	87	4.6	0.06	5.9	22	80	(9)	12.704	(1.3)	0.22955	(1.2)	386	(6)
2.2	c**	285	111	0.40	26.2	7	570	(11)	9.344	(1.1)	0.11366	(1.0)	615	(6)
3.1	r*	98	3.7	0.04	6.4	22	78	(8)	13.199	(1.3)	0.23231	(1.1)	370	(5)
3.2	c**	178	136	0.79	13.4	9	262	(16)	11.371	(1.2)	0.12734	(1.0)	498	(6)
4.1	c**	97	120	1.3	23.0	4	961	(15)	3.633	(1.2)	0.12853	(0.8)	1511	(17)
4.2	r*	110	4.8	0.04	7.6	20	86	(10)	12.482	(1.2)	0.21485	(1.3)	401	(5)
5.1	c**	157	53	0.35	17.1	8	364	(11)	7.880	(1.1)	0.13058	(0.9)	710	(8)
5.2	r*	28	1.2	0.04	2.0	26	87	(17)	11.994	(1.9)	0.26286	(2.0)	387	(8)
6.1	c**	210	147	0.72	37.8	5	979	(13)	4.773	(1.1)	0.12012	(0.6)	1172	(12)
6.2	r**	90	37	0.42	9.5	12	219	(12)	8.080	(1.2)	0.15943	(1.0)	667	(8)
7.1	r*	42	2.0	0.05	2.7	18	87	(14)	13.379	(1.7)	0.20093	(1.9)	383	(7)
8.1	r*	201	5.3	0.03	12.2	16	106	(7)	14.155	(1.1)	0.18243	(0.9)	372	(4)
9.1	c*	5	0.1	0.03	0.8	54	37	(18)	4.843	(3.5)	0.49833	(2.6)	590	(30)
10.1	r*	22	1.0	0.05	1.6	30	52	(14)	11.793	(2.3)	0.29563	(2.1)	372	(10)
11.1	r*	124	3.5	0.03	7.7	17	99	(8)	13.950	(1.2)	0.18778	(1.1)	374	(5)
11.2	c**	70	43	0.64	13.0	7	409	(14)	4.646	(1.3)	0.14092	(0.9)	1172	(14)
Sample 03-81. Pegmatite in boudin neck (UTM 27 0484416; 8666530)														
1.1	c*	3	0.02	0.01	0.8	76	22	(12)	3.279	(3.7)	0.67933	(2.2)	446	(46)
2.1	c*	28	0.9	0.03	2.3	42	44	(10)	10.411	(1.8)	0.38955	(1.6)	352	(9)
3.1	r*	37	1.4	0.04	2.7	35	62	(11)	11.761	(1.7)	0.33266	(1.5)	349	(7)
4.1	c	9	0.1	0.01	1.0	81	20	(10)	7.764	(2.6)	0.70070	(2.0)	152	(19)
7.1	r*	242	12	0.05	14.4	17	100	(6)	14.449	(1.1)	0.19242	(0.8)	359	(4)
8.1	c*	3	0.06	0.02	1.1	83	27	(13)	2.114	(4.1)	0.73527	(2.1)	509	(72)
9.1	c*	14	0.4	0.03	1.6	60	27	(10)	7.195	(2.2)	0.53684	(1.7)	350	(16)
Sample 03-39. Mylonite (UTM 27 0487195; 8665209)														
1.1	r*	282	16	0.06	16.1	16	125	(10)	15.004	(1.2)	0.18612	(1.1)	349	(4)
1.2	c*	123	3.0	0.03	9.4	43	51	(9)	11.240	(1.5)	0.39860	(1.2)	319	(7)
2.1	c*	103	2.5	0.03	8.8	46	42	(7)	10.014	(1.5)	0.42515	(1.2)	338	(8)
2.2	r*	253	12	0.05	14.4	17	89	(9)	15.016	(1.3)	0.18773	(1.2)	348	(5)
3.1	r*	253	16	0.07	14.9	17	120	(9)	14.604	(1.2)	0.18693	(1.4)	358	(5)
3.2	r*	164	5.0	0.03	11.2	30	60	(8)	12.654	(1.3)	0.29372	(1.1)	348	(6)
4.1	r*	255	16	0.06	14.7	16	123	(9)	14.897	(1.2)	0.18074	(1.2)	355	(5)
4.2	c*	80	1.1	0.01	7.4	50	37	(8)	9.238	(1.6)	0.45489	(1.5)	341	(10)
5.1	r*	234	12	0.05	13.2	15	113	(10)	15.194	(1.2)	0.17137	(1.2)	352	(5)
5.2	c*	117	2.6	0.02	9.6	43	45	(7)	10.473	(1.5)	0.40316	(1.1)	339	(8)
6.1	r*	253	14	0.06	13.5	15	135	(11)	16.145	(1.3)	0.17184	(1.3)	332	(4)
6.2	c*	74	0.6	0.01	7.2	57	32	(8)	8.813	(1.7)	0.51374	(1.3)	305	(11)
7.1	c*	100	2.8	0.03	8.3	44	45	(8)	10.367	(1.5)	0.40691	(1.7)	340	(9)
Sample 03-38. Storstrømmen shear zone mylonite (UTM 27 0493651; 8664168)														
1.1	c	77	181	2.4	4.9	15	144	(12)	13.572	(1.3)	0.17514	(1.5)	392	(6)
1.2	r*	2	0.06	0.03	0.9	81	19.4	(12)	2.105	(4.6)	0.72554	(2.4)	552	(77)
2.1	r*	3	0.35	0.11	0.8	75	23.1	(13)	3.502	(3.8)	0.66685	(2.3)	444	(44)
2.2	c	82	191	2.4	5.9	15	145	(11)	11.795	(1.3)	0.17878	(1.5)	448	(6)
3.1	r*	1	0.03	0.03	0.7	85	18.6	(12)	1.358	(6.0)	0.76633	(2.4)	674	(125)
4.1	c*	73	186	2.6	4.3	16	131	(13)	14.676	(1.4)	0.18108	(1.5)	360	(5)
4.2	c*	74	135	1.9	4.3	15	113	(12)	14.806	(1.5)	0.17762	(1.8)	358	(6)
5.1	c*	3	0.1	0.03	0.9	77	20.4	(12)	3.009	(3.9)	0.68477	(2.3)	476	(52)
6.1	c*	5	0.5	0.10	0.9	69	21.7	(12)	4.769	(3.2)	0.61140	(2.2)	412	(30)
7.1	c*	99	177	1.9	5.5	13	126	(12)	15.554	(1.3)	0.15573	(1.4)	352	(5)

(continued)

Table 3. U–Pb SHRIMP titanite geochronologic data and apparent ages *(continued)*.

Spot†		U§ (ppm)	Th (ppm)	Th/U	$^{206}Pb^{*}$§ (ppm)	$f^{206}Pb_c$§	$^{206}Pb/^{204}Pb$§		$^{238}U/^{206}Pb$#		$^{207}Pb/^{206}Pb$#		$^{206}Pb/^{238}U$†† (Ma)	
Sample 03-38. Storstrømmen shear zone mylonite (UTM 27 0493651; 8664168) *(continued)*														
8.1	c*	174	191	1.1	9.6	11	156	(10)	15.592	(1.2)	0.14503	(1.2)	357	(4)
Sample 03-68. Storstrømmen shear zone ultramylonite (UTM 27 0492815; 8659340)														
4.1		5	0.8	0.16	1.6	83	24.3	(10)	2.751	(3.1)	0.73168	(1.7)	381	(50)

Note: All analyses were performed on the SHRIMP–RG (sensitive high mass resolution ion microprobe – reverse geometry) ion microprobe at the United States Geological Survey–Stanford analytical facility, Stanford, CA.

† Spots reported as grain number-analysis number. c =core; r = rim. Annotations indicate analyses used in first (*) and second (**) age calculations.

§ Pb* denotes radiogenic Pb; Pb_c denotes common Pb; $f^{206}Pb_c = 100*(^{206}Pb_c/^{206}Pb_{total})$; errors in $^{206}Pb/^{204}Pb$ reported as percent at the 1 σ level.

Reported ratios are not corrected for common Pb. Errors are reported in parentheses as percent at the 1 σ level.

†† Ages calculated from ratios corrected for common Pb using ^{207}Pb-method for the $^{206}Pb/^{238}U$ age. Uncertainties in millions of years reported as 1 σ.

by exhumation to amphibolite-facies conditions starting by 395–390 Ma. Similarly, titanite from orthogneiss at Sanddal (03-76) dates Paleoproterozoic metamorphism or granite emplacement and Caledonian exhumation of the western block of the NEGEP through ca. 370 Ma. The clear preservation of Precambrian ages in titanite cores from the quartzofeldspathic gneisses that experienced T > 750°C during Caledonian HP metamorphism is consistent with recent estimates for a high closure temperature (> 800ºC) for titanite (Zhang and Scharer 1996; Gao et al. 2012; Kohn and Corrie 2011; Spencer et al. 2013). Caledonian metamorphic tectonites preserve evidence for deformation during HP metamorphism in eclogite and retrograde amphibolite-facies deformation in host gneiss during exhumation between 390 and 370 Ma. Interpretation of the SSZ as a narrow greenschist-facies deformation zone differs significantly from earlier descriptions of the SSZ as an 8 km-wide amphibolite- to greenschist-facies mylonitic shear zone (cf. Fig. 11; Smith et al. 2007) and decreases the inferred magnitude of displacement.

The timing of initial displacement on the SSZ is not documented and formation of the strike-slip shear zone during exhumation to amphibolite-facies conditions cannot be precluded. The lack of variation in protolith ages and estimated conditions and timing of HP metamorphism and decompression melting across the SSZ suggests that the structure largely formed after the initial exhumation of the NEGEP. U–Pb data from deformed titanite within the SSZ mylonite demonstrates on-going deformation after ca. 350 Ma. The SSZ was thus clearly active from the late Devonian well into the Carboniferous and most likely did not accommodate any Silurian sinistral translation.

Transpression Due to Sinistral Oblique Collision in the Greenland Caledonides?

The transpressional model for the SSZ is based on comparison of SSZ strike-slip deformation with thrusting observed in Dronning Louise Land (Holdsworth and Strachan 1991; Strachan et al. 1992; Smith et al. 2007). There is still no documented simultaneity in the time of thrusting in the foreland and movement on the SSZ. Linking the foreland and SSZ deformation based on $^{40}Ar/^{39}Ar$ data (Smith et al. 2007) is suspect because the observed cooling ages spanning from 400 to 380 Ma (Dallmeyer et al. 1994) in part overlap the time of HP metamorphism and are all much older than the time of SSZ displacement demonstrated herein. The $^{40}Ar/^{39}Ar$ ages are most likely plagued by excess argon (e.g. Giorgis et al. 2000). Better estimates for the timing of contraction in the foreland are required before models for synchronous displacement within a transpressional regime can be addressed. However, transpressional models are permissible for the SSZ since both the SSZ and foreland thrusting involve post-exhumation displacement of the NEGEP.

The available age constraints suggest that the SSZ was also synchronous with dextral displacement on the Germania Land deformation zone (GLDZ), which was active between 370 and 340 Ma (Sartini-Rideout et al. 2006) and has a conjugate relationship with the SSZ (Fig. 1). Simultaneous sinistral and dextral displacement on conjugate faults shows that the SSZ does not simply record oblique collision partitioned into sinistral strike-slip displacement and contraction in the foreland. Rather, the timing relations lead to an alternative model for lateral escape in the overriding plate during late Caledonian convergence (Gilotti and McClelland 2011).

Lateral Escape – An Alternative Scenario

The conjugate SSZ and GLDZ transect the NEGEP and are considered a part of a more regionally extensive array of strike-slip faults in the Greenland Caledonides. Important components of the fault system include the sinistral Western fault zone to the south in central East Greenland (Larsen and Bengaard 1991) and large vertical faults offshore to the east that bound the west side of the Danmarkshavn Basin (Hamann et al. 2005) along the Koldeway platform. Displacement on the SSZ and GLDZ is

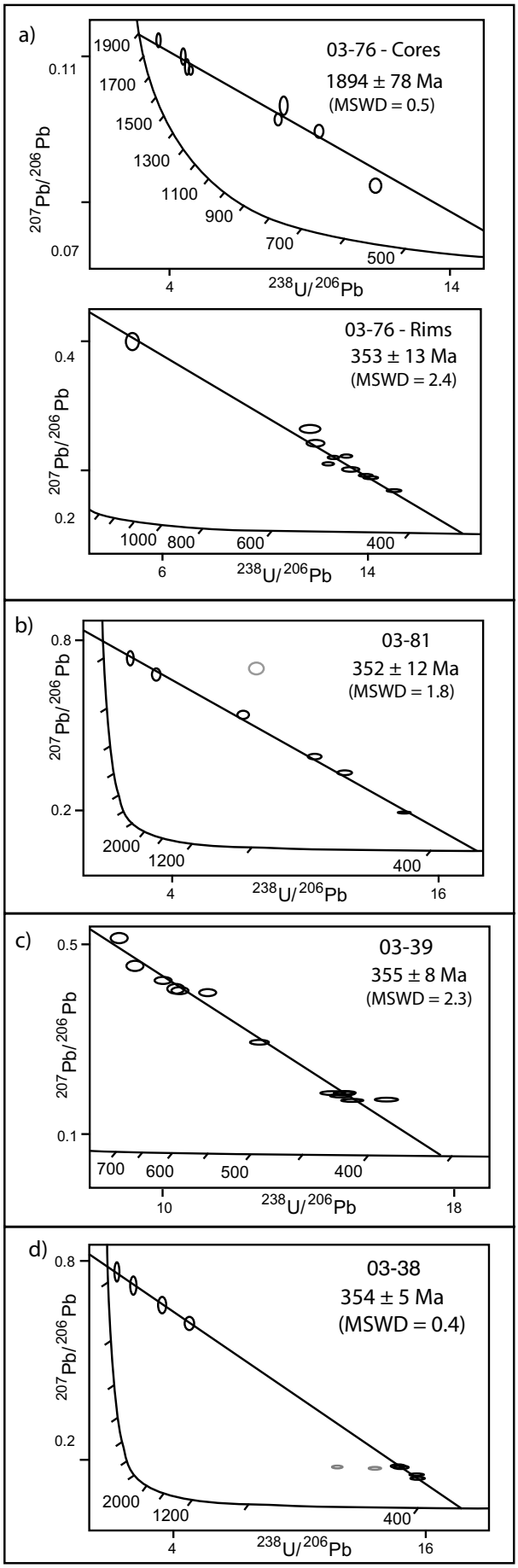

Figure 12. Tera–Wasserburg U–Pb plots for titanite SHRIMP-RG analyses from (a) granodioritic orthogneiss 03-76; (b) coarse grained pegmatite within a boudin neck 03-81; (c) garnet-bearing metagranitoid mylonite 03-39; (d) mylonite 03-38. Ellipses plotted at 1σ. Concordia intercept ages (95% confidence level) are determined by three-dimensional regressions with ellipses shown in light grey excluded from the regressions (see text for discussion). MSWD = mean square of weighted deviates.

broadly contemporaneous with the formation and exhumation of an ultra-high-pressure (UHP) terrane east of the GLDZ. The UHP terrane consists of a gneiss complex that is identical in protolith to other gneissic units of the NEGEP (Gilotti and McClelland 2011), but experienced UHP metamorphism at 365–350 Ma (McClelland et al. 2006; Gilotti et al. 2014), approximately 50 Ma after widespread HP metamorphism observed west of the GLSZ. The similarity in timing between strike-slip faulting and UHP metamorphism suggest that the strike-slip structures may be directly related to formation and exhumation of the North-East Greenland UHP terrane during intracontinental subduction of the overriding plate in a collisional orogen (Gilotti and McClelland 2007, 2011). In this context, the SSZ and GLDZ are interpreted to be relatively small features (see Fig. 13) with the main displacement leading to formation and exhumation of the UHP terrane occurring on larger structures located offshore to the east (Gilotti and McClelland 2011).

The model for intracratonic subduction in North-East Greenland is analogous in both timing and geometry to the intracratonic subduction suggested for present day Tibet (Tapponnier et al. 2001). The timing of Caledonian UHP metamorphism at 360 Ma, approximately 60–70 m.y. following the initial Baltica-Laurentia collision, is consistent with proposed, present day intracratonic subduction

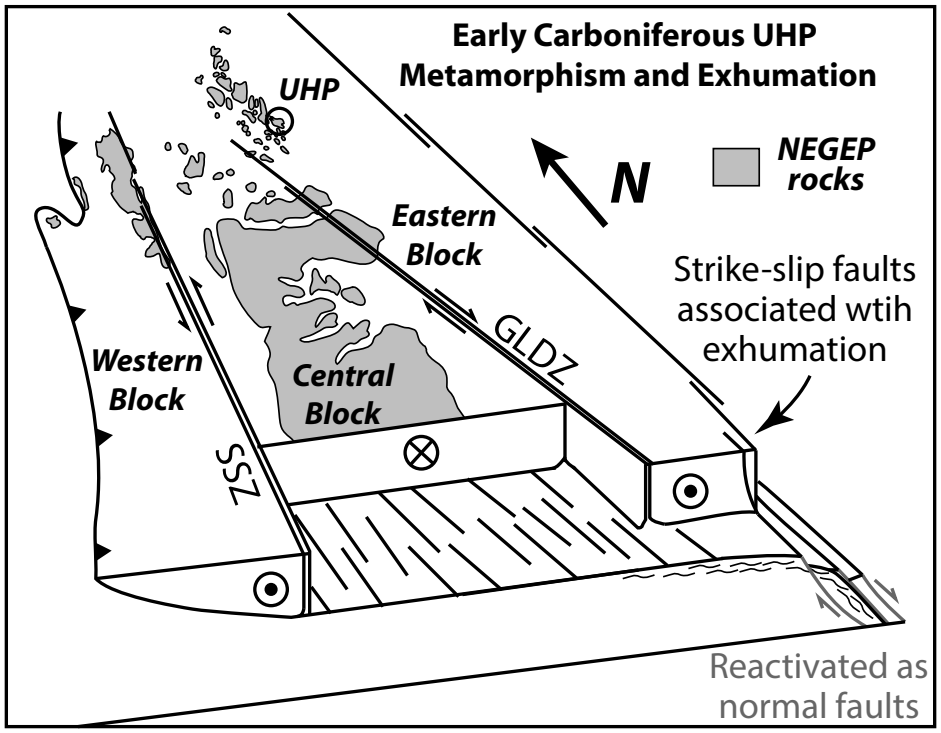

Figure 13. Simple cartoon block diagram depicting early Carboniferous lateral escape exhumation following UHP metamorphism in the eastern block of the North-East Greenland eclogite province (NEGEP).

beneath Tibet approximately 55 m.y. following the initial Himalayan collision. The geometry of conjugate strike-slip faults associated with formation and exhumation of UHP rocks in the Greenland Caledonides is similar to active faults in the Tibetan Plateau that can be interpreted as crustal scale faults associated with intracratonic subduction (Tapponnier et al. 2001). The Caledonian strike-slip faults are interpreted to have allowed lateral escape of material northward (present coordinates) as the Laurentia–Baltica continent-continent collision waned, similar to the extrusion of material out of Tibet and into the South China Sea in the present day India–Asia collision.

ACKNOWLEDGEMENTS

We thank Siobhán Power for her help with the fieldwork. Grants from the National Science Foundation to Gilotti (EAR-0208236 and EAR-1049433) and McClelland (EAR-0208158) supported this work. We are grateful to Joe Wooden, John Aleinikoff and Frank Mazdab for valuable discussions and their help with U–Pb analysis at the USGS–Stanford Ion Probe Lab (Stanford, CA).

REFERENCES

Aleinikoff, J.N., Wintsch, R.P., Fanning, C.M., and Dorais, M.J., 2002, U–Pb geochronology of zircon and polygenetic titanite from the Glastonbury Complex, Connecticut, USA: an integrated SEM, EMPA, TIMS, and SHRIMP study: Chemical Geology, v. 188, p. 125–147, http://dx.doi.org/10.1016/S0009-2541(02)00076-1.

Aleinikoff, J.N., Wintsch, R.P., Tollo, R.P., Unruh, D.M., Fanning C.M., and Schmitz, M.D., 2007, Ages and origins of rocks of the Killingworth dome, south-central Connecticut: Implications for the tectonic evolution of southern New England: American Journal of Science, v. 307, p. 63–118, http://dx.doi.org/10.2475/01.2007.04.

Barth, A.P., and Wooden, J.L., 2006, Timing of magmatism following initial convergence at a passive margin, southwestern U.S. Cordillera, and ages of lower crustal magma sources: The Journal of Geology, v. 114, p. 231–245, http://dx.doi.org/10.1086/499573.

Black, L.P., Kamo, S.L., Allen, C.M., Davis, D.W., Aleinikoff, J.N., Valley, J.W., Mundil, R., Campbell, I.H., Korsch, R.J., Williams, I.S., and Foudoulis, C., 2004, Improved $^{206}Pb/^{238}U$ microprobe geochronology by the monitoring of a trace-element-related matrix effect; SHRIMP, ID–TIMS, ELA–ICP–MS and oxygen isotope documentation for a series of zircon standards: Chemical Geology, v. 205, p. 115–140, http://dx.doi.org/10.1016/j.chemgeo.2004.01.003.

Brueckner, H.K., Gilotti, J.A., and Nutman, A.P., 1998, Caledonian eclogite-facies metamorphism of Early Proterozoic protoliths from the North-East Greenland Eclogite Province: Contributions to Mineralogy and Petrology, v. 130, p. 103–120, http://dx.doi.org/10.1007/s004100050353.

Dallmeyer, R.D., Strachan, R.A., and Henriksen, N., 1994, $^{40}Ar/^{39}Ar$ mineral age record in NE Greenland: implications for tectonic evolution of the North Atlantic Caledonides: Journal of the Geological Society, v. 151, p. 615–628, http://dx.doi.org/10.1144/gsjgs.151.4.0615.

DeMets, C., Gordon, R.G., Argus, D.F., and Stein, S., 1990, Current plate motions: Geophysical Journal International, v. 101, p. 425–478, http://dx.doi.org/10.1111/j.1365-246X.1990.tb06579.x.

Dewey, J.F., and Strachan, R.A., 2003, Changing Silurian–Devonian relative plate motion in the Caledonides: sinistral transpression to sinistral transtension: Journal of the Geological Society, v. 160, p. 219–229, http://dx.doi.org/10.1144/0016-764902-085.

Dewey, J.F., Holdsworth, R.E., and Strachan, R.A., 1998, Transpression and transtension zones, *in* Holdsworth, R.E., Strachan, R.A., and Dewey, J.F., *eds.*, Continental Transpressional and Transtensional Tectonics: Geological Society, London, Special Publications, v. 135, p. 1–14, http://dx.doi.org/10.1144/GSL.SP.1998.135.01.01.

Dutton, B.J., 1997, Finite strains in transpression zones with no boundary slip: Journal of Structural Geology, v. 19, p. 1189–1200, http://dx.doi.org/10.1016/S0191-8141(97)00043-6.

Elvevold, S., and Gilotti, J.A., 2000, Pressure–temperature evolution of retrogressed kyanite eclogites, Weinschenk Island, North-East Greenland Caledonides: Lithos, v. 53, p. 127–147, http://dx.doi.org/10.1016/S0024-4937(00)00014-1.

Fitch, T.J., 1972, Plate convergence, transcurrent faults, and internal deformation adjacent to Southeast Asia and the western Pacific: Journal of Geophysical Research, v. 77, p. 4432–4460, http://dx.doi.org/10.1029/JB077i023p04432.

Fossen, H., and Tikoff, B., 1993, The deformation matrix for simultaneous simple shearing, pure shearing and volume change, and its application to transpression-transtension tectonics: Journal of Structural Geology, v. 15, p. 413–422, http://dx.doi.org/10.1016/0191-8141(93)90137-Y.

Gao, Xiao-Ying, Zheng, Yong-Fei, Chen, Yi-Xang, Guo, Jingliang, 2012, Geochemical and U–Pb age constraints on the occurrence of polygenetic titanites in UHP metagranite in the Dabie orogen: Lithos, v. 136–139, p. 93–108, http://dx.doi.org/10.1016/j.lithos.2011.03.020.

Gilotti, J.A., 1993, Discovery of a medium-temperature eclogite province in the Caledonides of North-East Greenland: Geology, v. 21, p. 523–526, http://dx.doi.org/10.1130/0091-7613(1993)021<0523:DOAMTE>2.3.CO;2.

Gilotti, J.A., and McClelland, W.C., 2005, Leucogranites and the time of extension in the East Greenland Caledonides: The Journal of Geology, v. 113, p. 399–417, http://dx.doi.org/10.1086/430240.

Gilotti, J.A., and McClelland, W.C., 2007, Characteristics of, and a tectonic model for, ultrahigh-pressure metamorphism in the overriding plate of the Caledonian Orogen: International Geology Review, v. 49, p. 777–797, http://dx.doi.org/10.2747/0020-6814.49.9.777.

Gilotti, J.A., and McClelland, W.C., 2008, Geometry, kinematics, and timing of extensional faulting in the Greenland Caledonides—A synthesis, *in* Higgins, A.K., Gilotti, J.A., and Smith, M.P., *eds.*, The Greenland Caledonides: Evolution of the northeast margin of Laurentia: Geological Society of America Memoirs, v. 202, p. 251–271, http://dx.doi.org/10.1130/2008.1202(10).

Gilotti, J.A., and McClelland, W.C., 2011, Geochemical and geochronological evidence that the North-East Greenland ultrahigh-pressure terrane is Laurentian crust: The Journal of Geology, v. 119, p. 439–456, http://dx.doi.org/10.1086/660867.

Gilotti, J.A., Nutman, A.P., and Brueckner, H.K., 2004, Devonian to Carboniferous collision in the Greenland Caledonides: U–Pb zircon and SM–Nd ages of high-pressure and ultrahigh-pressure metamorphism: Contributions to Mineralogy and Petrology, v. 148, p. 216–235, http://dx.doi.org/10.1007/s00410-004-0600-4.

Gilotti, J.A., Jones, K.A., and Elvevold, S., 2008, Caledonian metamorphic patterns in Greenland, *in* Higgins, A.K., Gilotti, J.A., and Smith, M.P., *eds.*, The Greenland Caledonides: Evolution of the northeast margin of Laurentia: Geological Society of America Memoirs, v. 202, p. 201–225, http://dx.doi.org/10.1130/2008.1202(08).

Gilotti, J.A., McClelland, W.C., and Wooden, J.L., 2014, Zircon captures exhumation of an ultrahigh-pressure terrane, North-East Greenland Caledonides: Gondwana Research, v. 25, p. 235–256, http://dx.doi.org/10.1016/j.gr.2013.03.018.

Giorgis, D., Cosca, M., and Li, Shuguang, 2000, Distribution and significance of extraneous argon in UHP eclogite (Sulu terrain, China): insight from in situ $^{40}Ar/^{39}Ar$ UV-laser ablation analysis: Earth and Planetary Science Letters, v. 181, p. 605–615, http://dx.doi.org/10.1016/S0012-821X(00)00221-1.

Hamann, N.E., Whittaker, R.C., and Stemmerik, L., 2005, Geological development of the Northeast Greenland shelf, *in* Doré, A.G., and Vining, B.A., *eds.,* Petroleum geology: North-West Europe and Global Perspectives—Proceedings of the 6th Petroleum Geology Conference: Geological Society, London, p. 887–902.

Harland, W. B., 1971, Tectonic transpression in Caledonian Spitsbergen: Geological Magazine, v. 108, p. 27–42, http://dx.doi.org/10.1017/S0016756800050937.

Higgins, A.K., and Leslie, A.G., 2000, Restoring thrusting in the East Greenland Caledonides: Geology, v. 28, p. 1019–1022, http://dx.doi.org/10.1130/0091-7613(2000)28<1019:RTITEG>2.0.CO;2.

Higgins, A.K., and Leslie, A.G., 2008, Architecture and evolution of the East Greenland Caledonides—An introduction, *in* Higgins, A.K., Gilotti, J.A., and Smith, M.P., *eds.*, The Greenland Caledonides: Evolution of the Northeast Margin of Laurentia: Geological Society of America Memoirs, v. 202, p. 29–53, http://dx.doi.org/10.1130/2008.1202(02).

Holdsworth, R.E., and Strachan, R.A., 1991, Interlinked system of ductile strike slip and thrusting formed by Caledonian sinistral transpression in northeastern Greenland: Geology, v. 19, p. 510–513, http://dx.doi.org/10.1130/0091-7613(1991)019<0510:ISODSS>2.3.CO;2.

Hull, J.M., and Gilotti, J.A., 1994, The Germania Land deformation zone and related structures, North-East Greenland: Rapport om Grønlands Geologiske Undersøgelse, v. 162, p. 113–127.

Hull, J.M., Friderichsen, J.D., Gilotti, J.A., Henriksen, N., Higgins, A.K., and Kalsbeek, F., 1994, Gneiss complex of the Skærfjorden region, North-East Greenland: Rapport om Grønlands Geologiske Undersøgelse, v. 162, p. 35–51.

Hurst, J.M., McKerrow, W.S., Soper, N.J., and Surlyck, F., 1983, The relationship between Caledonian nappe tectonics and Silurian turbidite deposition in North Greenland: Journal of the Geological Society, v. 140, p. 123–131, http://dx.doi.org/10.1144/gsjgs.140.1.0123.

Jiang, Dazhi, and Williams, P.F., 1998, High-strain zones; a unified model: Journal of Structural Geology, v. 20, p. 1105–1120, http://dx.doi.org/10.1016/S0191-8141(98)00025-X.

Jones, R.R., and Tanner, P.W.G., 1995, Strain partitioning in transpression zones: Journal of Structural Geology, v. 17, p. 793–802, http://dx.doi.org/10.1016/0191-8141(94)00102-6.

Jones, R.R., Holdsworth, R.E., and Bailey, W., 1997, Lateral extrusion in transpression zones: the importance of boundary conditions: Journal of Structural Geology, v. 19, p. 1201–1217, http://dx.doi.org/10.1016/S0191-8141(97)00034-5.

Jones, R.R., Holdsworth, R.E., Clegg, P., McCaffrey, K., and Tavarnelli, E., 2004, Inclined transpression: Journal of Structural Geology, v. 26, p. 1531–1548, http://dx.doi.org/10.1016/j.jsg.2004.01.004.

Kalsbeek, F., Nutman, A.P., Escher, J.C., Friderichsen, J.D., Hull, J.M., Jones, K.A., and Schack Pedersen, S.A., 1999, Geochronology of granitic and supracrustal rocks from the northern part of the East Greenland Caledonides: ion microprobe U–Pb zircon ages: Geology of Greenland Survey Bulletin, v. 184, p. 31–48.

Kalsbeek, F., Thrane, K., Higgins, A.K., Jepsen, H.F., Leslie, A.G., Nutman, A.P., and Frie, R., 2008, Polyorogenic history of the East Greenland Caledonides, *in* Higgins, A.K., Gilotti, J.A., and Smith, M.P., *eds.*, The Greenland Caledonides: Evolution of the Northeast Margin of Laurentia: Geological Society of America Memoirs, v. 202, p. 55–72, http://dx.doi.org/10.1130/2008.1202(03).

Kohn, M.J., and Corrie, S.L., 2011, Preserved Zr-temperatures and U–Pb ages in high-grade metamorphic titan-

ite: Evidence for a static hot channel in the Himalayan orogen: Earth and Planetary Science Letters, v. 311, p. 136–143, http://dx.doi.org/10.1016/j.epsl.2011.09.008.

Lang, H.M., and Gilotti, J.A., 2001, Plagioclase replacement textures in partially eclogitised gabbros from the Sanddal mafic–ultramafic complex, Greenland Caledonides: Journal of Metamorphic Geology, v. 19, p. 497–517, http://dx.doi.org/10.1046/j.0263-4929.2001.00325.x.

Larsen, P.-H., and Bengaard, H.-J., 1991, Devonian basin initiation in East Greenland: A result of sinistral wrench faulting and Caledonian extensional collapse: Journal of the Geological Society, v. 148, p. 355–368, http://dx.doi.org/10.1144/gsjgs.148.2.0355.

Leslie, A.G., and Higgins, A.K., 2008, Foreland-propagating Caledonian thrust systems in East Greenland, *in* Higgins, A.K., Gilotti, J.A., and Smith, M.P., *eds.*, The Greenland Caledonides: Evolution of the Northeast Margin of Laurentia: Geological Society of America Memoirs, v. 202, p. 169–199, http://dx.doi.org/10.1130/2008.1202(07).

Lin, Shoufa, Jiang, Dazhi, and Williams, P.F., 1998, Transpression (or transtension) zones of triclinic symmetry: natural example and theoretical modeling, *in* Holdsworth, R.E., Strachan, R.A. and Dewey, J.F., *eds.*, Continental Transpressional and Transtensional Tectonics: Geological Society, London, Special Publications, v. 135, p. 41–57, http://dx.doi.org/10.1144/GSL.SP.1998.135.01.04.

Ludwig, K.R., 1998, On the treatment of concordant uranium–lead ages: Geochimica et Cosmochimica Acta, v. 62, p. 665–676, http://dx.doi.org/10.1016/S0016-7037(98)00059-3.

Ludwig, K.R., 2001, Squid version 1.02: A user's manual: Berkeley Geochronology Center Special Publication, v. 2, p. 1–22.

Ludwig, K.R., 2003, User's manual for Isoplot 3.00: a geochronological toolkit for Microsoft Excel: Berkeley Geochronology Center Special Publication No. 4, Berkeley, USA, 70 p.

Mattinson, J.M., 2010, Analysis of the relative decay constants of ^{235}U and ^{238}U by multi-step CA–TIMS measurements of closed-system natural zircon samples: Chemical Geology, v. 275, p. 186–198, http://dx.doi.org/10.1016/j.chemgeo.2010.05.007.

McClelland, W.C., Power, S.E., Gilotti, J.A., Mazdab, F.K., and Wopenka, B., 2006, U–Pb SHRIMP geochronology and trace-element geochemistry of coesite-bearing zircons, North-East Greenland Caledonides, *in* Hacker, B.,R. McClelland, W.C., and Liou, J.G., *eds.*, Ultrahigh-pressure metamorphism: Deep continental subduction: Geological Society of America Special Papers, v. 403, p. 23–43, http://dx.doi.org/10.1130/2006.2403(02).

Molnar, P., 1992, Chapter 18 Brace-Goetze strength profiles, the partitioning of strike-slip and thrust faulting at zones of oblique convergence, and the stress-heat flow paradox of the San Andreas Fault: International Geophysics, v. 51, p. 435–459, http://dx.doi.org/10.1016/S0074-6142(08)62833-8.

Nutman, A.P., and Kalsbeek, F., 1994, Search for Archean basement in the Caledonian fold belt of North-East Greenland: Rapport om Grønlands Geologiske Undersøgelse, v. 162, p. 129–133.

Oldow, J.S., Bally, A.W., and Avé Lallemant, H.G., 1990, Transpression, orogenic float, and lithospheric balance: Geology, v. 18, p. 991–994, http://dx.doi.org/10.1130/0091-7613(1990)018<0991:TOFALB>2.3.CO;2.

Rasmussen, J.A., and Smith, M.P., 2001, Conodont geothermometry and tectonic overburden in the northernmost East Greenland Caledonides: Geological Magazine, v. 138, p. 687–698, http://dx.doi.org/10.1017/S0016756801005908.

Sanderson, D.J., and Marchini, W.R.D., 1984, Transpression: Journal of Structural Geology, v. 6, p. 449–458, http://dx.doi.org/10.1016/0191-8141(84)90058-0.

Sartini-Rideout, C., Gilotti, J.A., and McClelland, W.C., 2006, Geology and timing of dextral strike-slip shear zones in Danmarkshavn, North-East Greenland Caledonides: Geological Magazine, v. 143, p. 431–446, http://dx.doi.org/10.1017/S0016756806001968.

Sartini-Rideout, C., Gilotti, J.A., and McClelland, W.C., 2009, Reaction progress and timing of retrogression of eclogite-facies rocks, Danmarkshavn, North-East Greenland Caledonides: European Journal of Mineralogy, v. 21, p. 1149–1172, http://dx.doi.org/10.1127/0935-1221/2009/0021-2002.

Sibson, R.H., 1977, Fault rocks and fault mechanisms: Journal of the Geological Society, v. 133, p. 191–213, http://dx.doi.org/10.1144/gsjgs.133.3.0191.

Smith, S.A.F., Strachan, R.A., and Holdsworth, R.E., 2007, Microstructural evolution within a partitioned midcrustal transpression zone, northeast Greenland Caledonides: Tectonics, v. 26, TC4003, http://dx.doi.org/10.1029/2006TC001952.

Soper, N.J., and Hutton, D.H.W., 1984, Late Caledonian sinistral displacements in Britain: Implications for a three-plate collision model: Tectonics, v. 3, p. 781–794, http://dx.doi.org/10.1029/TC003i007p00781.

Soper, N.J., Strachan, R.A., Holdsworth, R.E., Gayer, R.A., and Greiling, R.O., 1992, Sinistral transpression and the Silurian closure of Iapetus: Journal of the Geological Society, v. 149, p. 871–880, http://dx.doi.org/10.1144/gsjgs.149.6.0871.

Spencer, K.J., Hacker, B.R., Kylander-Clark, A.R.C., Andersen, T.B., Cottle, J.M., Stearns, M.A., Poletti, J.E., and Seward, G.G.E., 2013, Campaign-style titanite U–Pb dating by laser-ablation ICP: Implications for crustal flow, phase transformations and titanite closure: Chemical Geology, v. 341, p. 84–101, http://dx.doi.org/10.1016/j.chemgeo.2012.11.012.

Stacey, J.S., and Kramers, J.D., 1975, Approximation of terrestrial lead isotope evolution by a two-stage model: Earth and Planetary Science Letters, v. 26, p. 207–221, http://dx.doi.org/10.1016/0012-821X(75)90088-6.

Strachan, R.A., and Tribe, I.R., 1994, Structure of the Storstrømmen Shear Zone, eastern Hertugen af Orléans Land, North-East Greenland: Rapport om Grønlands Geologiske Undersøgelse, v.162, p. 103–112.

Strachan, R.A., Jepsen, H.F., and Kalsbeek, F., 1991, Regional Caledonian structure of Hertugen af Orléans Land, North-East Greenland: Rapport om Grønlands Geologiske Undersøgelse, v. 152, p. 95–102.

Strachan, R.A., Holdsworth, R.E., Friderichsen, J.D., and Jepsen, H.F., 1992, Regional Caledonian structure within an oblique convergence zone, Dronning Louise Land, NE Greenland: Journal of the Geological Society, v. 149, p. 359–371, http://dx.doi.org/10.1144/gsjgs.149.3.0359.

Strachan, R.A., Chadwick, B., Friend, C.R.L., and Holdsworth, R.E., 1995, New perspectives on the Caledonian Orogeny in Northeast Greenland, *in* Hibbard, J.P., van Staal, C.R., and Cawood, P.A., *eds.*, Current perspectives in the Appalachian–Caledonian Orogen: Geological Association of

Canada Special Paper 41, p. 303–320.
Tapponnier, P., Zhiqin, Xu, Roger, F., Meyer, B., Arnaud, N., Wittlinger, G., and Yang, Jingsui, 2001, Oblique stepwise rise and growth of the Tibet Plateau: Science, v. 294, p. 1671–1677, http://dx.doi.org/10.1126/science.105978.
Teyssier, C., Tikoff, B., and Markley, M., 1995, Oblique plate motion and continental tectonics: Geology, v. 23, p. 447–450, http://dx.doi.org/10.1130/0091-7613(1995)023<0447:OPMACT>2.3.CO;2.
Tikoff, B., and Greene, D., 1997, Stretching lineations in transpressional shear zones: an example from the Sierra Nevada Batholith, California: Journal of Structural Geology v. 19, p. 29–39, http://dx.doi.org/10.1016/S0191-8141(96)00056-9.
Tikoff, B., and Teyssier, C., 1994, Strain modeling of displacement-field partitioning in transpressional orogens: Journal of Structural Geology, v. 16, p. 1575–1588, http://dx.doi.org/10.1016/0191-8141(94)90034-5.
Whitney, D.L., and Evans, B.W., 2010, Abbreviations for names of rock-forming minerals: American Mineralogist, v. 95, p. 185–187, http://dx.doi.org/10.2138/am.2010.3371.
Williams, I.S., 1998, U–Pb by ion microprobe, *in* McKibben M.A., Shanks, W.C., and Ridley, W.I., *eds.*, Applications of microanalytical techniques to understanding mineralizing processes: Society of Economic Geologists Reviews in Economic Geology 7, p. 1–35.
Zhang, Lian-Sheng, and Schärer, U., 1996, Inherited Pb components in magmatic titanite and their consequence for the interpretation of U–Pb ages: Earth and Planetary Science Letters, v. 138, p. 57–65, http://dx.doi.org/10.1016/0012-821X(95)00237-7.

Received July 2013
Accepted as revised December 2013
First published on the web
February 2014